

A stellar dynamical mass measure of an inactive black hole in the distant universe

Andrew B. Newman^{1*}, Meng Gu², Sirio Belli³, Richard S. Ellis⁴,
 Sai Gangula^{5,1}, Jenny E. Greene⁶, Jonelle L. Walsh⁷, Sherry H. Suyu^{8,9},
 Sebastian Ertl^{9,8}, Gabriel Caminha^{9,8}, Giovanni Granata^{10,11,12}, Claudio Grillo^{10,13},
 Stefan Schuldt^{10,13}, Tania M. Barone¹⁴, Simeon Bird¹⁵, Karl Glazebrook¹⁴,
 Marziye Jafariyazani¹⁶, Mariska Kriek¹⁷, Allison Matthews¹, Takahiro Morishita¹⁸,
 Themiya Nanayakkara¹⁴, Justin D. R. Pierel¹⁹, Ana Acebrón^{20,13}, Pietro Bergamini^{10,21},
 Sangjun Cha²², Jose M. Diego²⁰, Nicholas Foo²³, Brenda Frye²⁴,
 Yoshinobu Fudamoto^{25,24}, M. James Jee^{22,26}, Patrick S. Kamienieski²³,
 Anton M. Koekemoer¹⁹, Asish K. Meena²⁷, Shun Nishida²⁸, Masamune Oguri^{25,28},
 Piero Rosati^{11,21}, Adi Zitrin²⁷

¹Observatories, Carnegie Science, Pasadena, CA 91101, USA.

²Department of Physics, University of Hong Kong, Hong Kong, China.

³Dipartimento di Fisica e Astronomia, Università di Bologna, Bologna 40129, Italy.

⁴Department of Physics & Astronomy, University College London, London WC1E 6BT, UK.

⁵Department of Physics and Astronomy, University of Southern California, Los Angeles, CA 90089, USA.

⁶Department of Astrophysical Sciences, Princeton University, Princeton, NJ 08544, USA.

⁷George P. and Cynthia Woods Mitchell Institute for Fundamental Physics and Astronomy,
 Department of Physics and Astronomy, Texas A&M University, College Station, TX 77843, USA.

⁸TUM School of Natural Sciences, Technical University of Munich, Garching 85748, Germany.

⁹Max-Planck-Institut für Astrophysik, Garching 85748, Germany.

¹⁰Dipartimento di Fisica, Università degli Studi di Milano, Milano I-20133, Italy.

¹¹Dipartimento di Fisica e Scienze della Terra, Università degli Studi di Ferrara, Ferrara I-44122, Italy.

¹²Institute of Cosmology and Gravitation, University of Portsmouth, Portsmouth PO1 3FX, UK.

¹³INAF-IASF, Istituto di Astrofisica Spaziale e Fisica cosmica Milano, Milano I-20133, Italy.

¹⁴Centre for Astrophysics and Supercomputing, Swinburne University of Technology, Hawthorn,
 Victoria 3122, Australia.

¹⁵Department of Physics & Astronomy, University of California Riverside, Riverside, CA 92521, USA.

¹⁶SETI Institute, Mountain View, CA 94043, USA.

¹⁷Leiden Observatory, Leiden University, Leiden 2300 RA, The Netherlands.

¹⁸IPAC, California Institute of Technology, Pasadena, CA 91125, USA.

¹⁹Space Telescope Science Institute, Baltimore, MD 21218, USA.

²⁰Instituto de Física de Cantabria (CSIC-UC), Santander 39005, Spain.

²¹INAF–OAS, Osservatorio di Astrofisica e Scienza dello Spazio di Bologna, Bologna I-40129, Italy.

²²Department of Astronomy, Yonsei University, Seoul 03722, Korea.

²³School of Earth and Space Exploration, Arizona State University, Tempe, AZ 85287, USA.

²⁴Department of Astronomy and Steward Observatory, University of Arizona, Tucson, AZ 85721, USA.

²⁵Center for Frontier Science, Chiba University, Chiba 263-8522, Japan.

²⁶Department of Physics and Astronomy, University of California Davis, Davis, CA 95616, USA.

²⁷Department of Physics, Ben-Gurion University of the Negev, Be'er-Sheva 84105, Israel.

²⁸Department of Physics, Graduate School of Science, Chiba University, Chiba 263-8522, Japan.

*Corresponding author. Email: anewman@carnegiescience.edu

Understanding the coevolution of supermassive black holes and their host galaxies requires tracing their growth over time. Mass measurements of distant black holes have been limited to active nuclei and commonly rely on spatially unresolved observations, leading to large uncertainties. Accurate masses can be determined by resolving the kinematics of stars within the sphere of influence, which has heretofore been possible only in the local universe. Using JWST, we have measured the mass $M_{\bullet} = 6.0^{+2.1}_{-1.7} \times 10^9 M_{\odot}$ of an inactive black hole in a gravitationally lensed quiescent galaxy at redshift $z = 1.95$, along with detailed host properties. Comparisons to local galaxies suggest that the correlation between M_{\bullet} and bulge mass has evolved substantially, whereas the correlation with stellar velocity dispersion may have been in place for 10 Gyr.

Studies of the intertwined growth of supermassive black holes and their host galaxies are grounded in empirical correlations between the black hole mass M_{\bullet} and host galaxy properties (1–3). Determining the evolution of these correlations requires measuring accurate masses for distant black holes. The masses of black holes in the distant universe have been estimated based on the kinematics of gas within the broad-line region of actively accreting systems. This region spans tens of microarcseconds or less and has been resolved only in one distant quasar (4). Most commonly, virial mass estimators (5) are applied to emission line widths and luminosities measured in unresolved spectra. However, this approach relies on estimates of the size and structure of the broad-line region, resulting in large uncertainties of up to an order of magnitude (4, 6).

Measuring the properties of distant galaxies that host active black holes is also challenging, especially for the most massive black holes identified as quasars, as they greatly outshine their hosts. Observing inactive black holes facilitates studies of the host galaxies and permits robust mass determinations via stellar dynamical methods. But at $z \gtrsim 0.3$, such methods require a spatial resolution of tens of milliarcseconds or better to resolve the black hole’s sphere of influence. Consequently the most reliable black hole mass measurements have been limited to distances < 200 Mpc (7).

Observations and galaxy properties

JWST can resolve the sphere of influence of very massive black holes in distant galaxies that are highly magnified by gravitational lensing. The most promising such system is the quiescent galaxy MRG-M0138 at $z = 1.95$ (8), which is extremely bright, highly magnified, and dominated by an old stellar population with minimal dust extinction, which facilitates stellar kinematic measurements. We observed MRG-M0138 using the NIRSpect integral field unit (IFU) onboard JWST. The observations targeted one of the multiple images (Fig. 1A) using two gratings, covering the rest-frame wavelength range $\lambda_{\text{rest}} = 0.33\text{--}1.07 \mu\text{m}$ at a resolving power of $R \sim 1000$. Gravitational magnification by a factor $\mu = 29_{-11}^{+13}$ provided a resolution of $\sigma_{\text{psf}} = 91 \text{ pc}$ at the galaxy center (9). Images obtained using the Hubble Space Telescope and JWST’s NIRCcam span $\lambda_{\text{rest}} = 0.19\text{--}1.5 \mu\text{m}$ using 7 filters.

Reconstructing the NIRCcam images in the source plane (Fig. 1B) reveals a multi-component structure: an inclined disk contributes 62% of the light in the F200W filter, with the remainder from a compact and rounder bulge. High-quality spectra were extracted in 219 spatial bins (not all independent; (9)), a major increase over previous resolved kinematics of high-redshift quiescent galaxies (10–13). We used stellar population synthesis (SPS) techniques to model the binned spectra together with the photometry, resulting in maps of the stellar velocity V (Fig. 1C), the velocity dispersion σ (Fig. 1D), and the stellar mass distribution. MRG-M0138 is a massive and dense galaxy: its total stellar mass is $M_{*,\text{MW}} = 2.2_{-0.7}^{+1.4} \times 10^{11} M_{\odot}$, based on SPS modeling assuming a Milky Way stellar initial mass function (IMF) (14); its half-light semi-major axis is $R_e = 2.7_{-0.5}^{+0.8} \text{ kpc}$, typical of quiescent galaxies of its mass and redshift (15); and it has a high effective velocity dispersion of $\sigma_e = 398 \pm 12 \text{ km s}^{-1}$ within the bulge effective radius $R_{e,\text{bulge}} = 0.8_{-0.1}^{+0.2} \text{ kpc}$.

Black hole mass and Eddington ratio

We modeled the stellar dynamics using Jeans anisotropic modeling (JAM, (16)), a technique that has been shown to produce accurate M_{\bullet} estimates in fast-rotator galaxies like MRG-M0138 (17). The stellar mass distributions of the bulge and disk were calculated using our SPS fits, which account for gradients in age, metallicity, and dust. Our dynamical models allow for a non-Milky Way IMF with possible spatial gradients, gradients in the velocity anisotropy, a black hole, and dark matter. The fiducial model provides a good fit to the projected second velocity moment $V_{\text{rms}} = \sqrt{V^2 + \sigma^2}$, whereas a model without a black hole cannot match the central V_{rms} peak (Fig. 2). A suite of dynamical models that varied key uncertain assumptions produced consistent M_{\bullet} estimates (9), which we combined using Bayesian model averaging.

We measured the black hole mass to be $\log M_{\bullet}/M_{\odot} = 9.78_{-0.12}^{+0.08} (\text{stat.})_{-0.09}^{+0.11} (\text{sys.})$, or $\log M_{\bullet}/M_{\odot} = 9.78_{-0.15}^{+0.13}$ if combining the statistical and systematic components in quadrature. The systematic error budget includes several sources (9), with the largest contribution being uncertainty in the lensing magnification. The radius of the black hole sphere of influence, $r_{\text{inf}} = GM_{\bullet}/\sigma^2 = 164 \text{ pc}$, is resolved by a factor $r_{\text{inf}}/\sigma_{\text{psf}} = 1.8$, similar to observations of nearby lower-mass black holes (17). The models also provided dynamical masses for the bulge stars, $M_{\text{bulge}} = 1.0_{-0.2}^{+0.3} \times 10^{11} M_{\odot}$, and for the total stellar system, $M_{\text{stars}} = 2.5_{-0.6}^{+0.9} \times 10^{11} M_{\odot}$.

The gravitational magnification further enabled us to isolate the nuclear spectrum within $r \approx 100 \text{ pc}$ and place limits on the active galactic nucleus (AGN) bolometric luminosity L_{bol} . Faint emission lines were detected with ratios indicative of a low-ionization nuclear emission region

(LINER). The upper limit we derived on the $H\alpha$ luminosity implies $L_{\text{bol}} < 10^{42.8}$ erg s $^{-1}$ and $\lambda_{\text{Edd}} = L_{\text{bol}}/L_{\text{Edd}} < 10^{-5.1}$. A non-detection by the Chandra X-ray Observatory gives an upper limit that is 0.7 dex weaker (9). MRG-M0138 has therefore reached the low Eddington ratios seen in typical local galaxies, which are thought to be undergoing radiatively inefficient accretion (18). It is the only inactive black hole at a high redshift for which a dynamical mass has been measured; all other such measurements were based on broad lines observed in active systems, which we define as $\lambda_{\text{Edd}} \gtrsim 0.01$ (Fig. 3A).

Black hole scaling relations

Remarkably, the MRG-M0138 black hole is as massive as the engines of rare luminous quasars (Fig. 3A-B). Whereas quasars are identified based on their high luminosities, which is understood to preferentially select massive black holes, this outcome was not preordained in MRG-M0138. Its mass fraction $M_{\bullet}/M_{\text{stars}} = 0.024_{-0.007}^{+0.008}$ is an order of magnitude higher than the average of coeval faint AGN (19). It is also among the highest $M_{\bullet}/M_{\text{stars}}$ typically observed in local galaxies (Fig. 3B). A comparison of cosmological simulations shows that they rarely produce $z = 2$ galaxies matching both the well-constrained M_{\bullet} and M_{stars} of MRG-M0138 (20). Considering specifically the ASTRID simulation, it contains 635 galaxies at $z = 2$ that match the stellar mass of MRG-M0138 (within 1σ of M_{stars}), but only 2 contain a black hole as massive (within 1σ of M_{\bullet} , or higher) (21). Compared to the TRINITY model, MRG-M0138 is a factor of 5 above the median $M_{\bullet}-M_{\text{stars}}$ relation at $z = 2$, corresponding to a 2–3 σ outlier (22). Along with JWST detections of overmassive black holes at higher redshifts (23–28), our results indicate that early black hole growth proceeded very efficiently in some systems.

The origin of the high M_{\bullet} in MRG-M0138 may be related to its density, as indicated by its extremely high σ_e . MRG-M0138 already lies on the local $M_{\bullet}-\sigma$ relation (Fig. 3D). Together with evidence from studies using gas emission lines as proxies for σ (27), our measurements suggest that this relation is fundamental and may have evolved little. Although it must be verified using larger samples, a weak or null evolution of the $M_{\bullet}-\sigma$ relation is a critical constraint on models of black hole growth, as the predictions of cosmological simulations vary widely (29, 30). Our measurement is also an indirect test of broad-line mass estimates at $z > 2$: if the $M_{\bullet}-\sigma$ relation does not significantly evolve, σ can be used to estimate M_{\bullet} at high redshifts. Such an estimate is compatible with the broad-line-based M_{\bullet} estimates in the two quiescent galaxies at $z \approx 2-5$ for which both measurements have been made (Fig. 3D) (31, 32).

Despite its consistency with the local $M_{\bullet}-\sigma$ relation, MRG-M0138 is an outlier from the local $M_{\bullet}-M_{\text{bulge}}$ relation of early-type galaxies (Fig. 3C), which has a similar scatter to the $M_{\bullet}-\sigma$ relation (1) and is often used interchangeably. Our measurements suggest that the $M_{\bullet}-M_{\text{bulge}}$ relation has evolved far more. This is understandable in light of observations that many of the stars in massive ellipticals today were not in bulges during the main period of black hole growth, as indicated by the more disk-like morphologies and kinematics (12) of early quiescent galaxies. Similar conclusions on the evolution of the $M_{\bullet}-M_{\text{bulge}}$ relation were reached by studies of quasar hosts in which M_{bulge} , though not directly measurable, was estimated statistically (33).

Implications for evolutionary pathways

The MRG-M0138 black hole likely grew mainly by radiatively efficient accretion (34). Assuming a typical $\lambda_{\text{Edd}} \sim 0.3$ (35), its luminosity reached $L_{\text{bol}} \approx 10^{47}$ erg s⁻¹. Such luminous quasars often drive winds with gas outflow rates of $\sim 10^3 M_{\odot} \text{ yr}^{-1}$ (36). Thus our M_{\bullet} measurement indicates that MRG-M0138 was likely a site of powerful AGN feedback. Although we cannot causally link such activity to the quenching of star formation and the low observed gas fraction (37), MRG-M0138 may have evolved as envisioned by theoretical models that propose a merger-induced starburst and quasar phase as the origin of massive elliptical galaxies (38). A major merger would have destroyed the stellar disks of the progenitors, but that is not necessarily incompatible with the thin stellar disk we observe in MRG-M0138. Merger simulations predict that when the gas fraction is high, as observed at high redshifts, a substantial fraction of the gas will not be consumed in the starburst and will reform a disk (38, 39).

Though not yet an elliptical galaxy, MRG-M0138 will likely become one: its mass is already $M_{\text{stars}} \approx 10^{11.4} M_{\odot}$, which is expected to double between $z = 2$ and 0 primarily due to mergers (40), placing it in a mass regime dominated by slowly rotating, elliptical galaxies today (41). If the mergers are gas-poor, they are not expected to produce significant black hole growth (42) nor to greatly change σ (43). Merger-driven growth of MRG-M0138 may therefore maintain its consistency with the local $M_{\bullet}-\sigma$ relation (Fig. 3D) while evolving it toward the mean $M_{\bullet}-M_{\text{stars}}$ relation (Fig. 3B) of the early types. To form an elliptical, mergers must also redistribute stars from the stellar disk into a bulge; together with the expected mass doubling, this evolutionary path would bring MRG-M0138 onto the local $M_{\bullet}-M_{\text{bulge}}$ relation (dashed line with arrow in Fig. 3C), with final black hole and stellar masses similar to M87 (44, 45).

A class of “relic” galaxies in the local universe have similar structural and stellar population properties to quiescent galaxies at $z > 2$ and are proposed to be rare instances of such systems that escaped mergers and survived intact to the present day (46). We can now directly test this proposition by comparing the resolved stellar kinematics and M_{\bullet} of the relics to MRG-M0138. Its rapidly rotating disk and peaked central velocity dispersion strongly resemble the kinematics of the relics (47, 48). High-resolution stellar dynamical measures indicate that the relics are outliers on the $M_{\bullet}-M_{\text{bulge}}$ relation but not the $M_{\bullet}-\sigma$ relation (49–54), like MRG-M0138 (Figs. 3C-D). Our detailed observations of MRG-M0138 support the interpretation of relics as relatively unaltered descendants of early quiescent galaxies.

MRG-M0138 provides a glimpse of the dominant, inactive population of massive black holes in the distant universe. Larger samples will be needed to map the demographics of these black holes and understand their coevolution, if any, with their host galaxies. Further observations of lensed quiescent galaxies may provide additional insights, while 30 m-class telescopes will be able to resolve the sphere of influence of the most massive black holes at any distance, even without the aid of gravitational lensing.

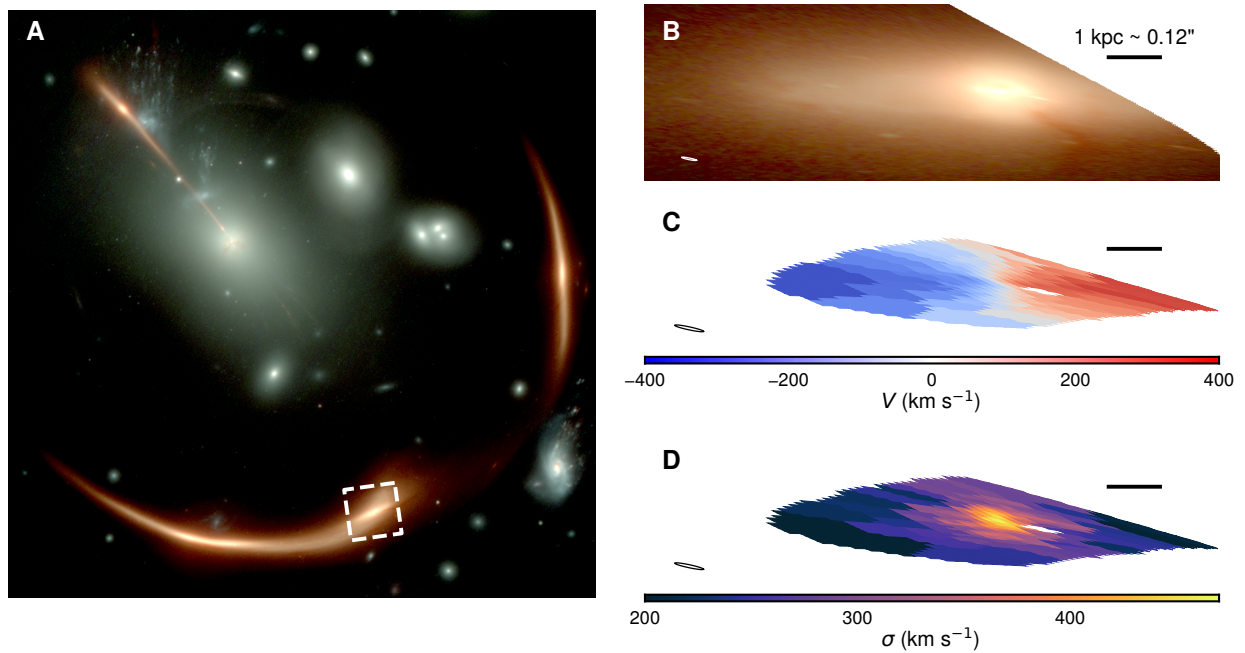


Figure 1: Structure and stellar kinematics of the massive, highly magnified galaxy MRG-M0138. (A) JWST/NIRCam image of the lensing galaxy cluster MACS J0138.0–2155 through the F115W, F150W, and F356W filters, displayed with a logarithmic stretch. MRG-M0138 is the bright, red, multiply imaged galaxy. The dashed box shows the NIRSpec IFU field of view. (B) Reconstructed image of the galaxy in the source plane. (C) Stellar velocity V map. (D) Stellar velocity dispersion σ map. The size of the point spread function (PSF) is shown in the lower-left corner of **B** (NIRCam) and **C-D** (NIRSpec).

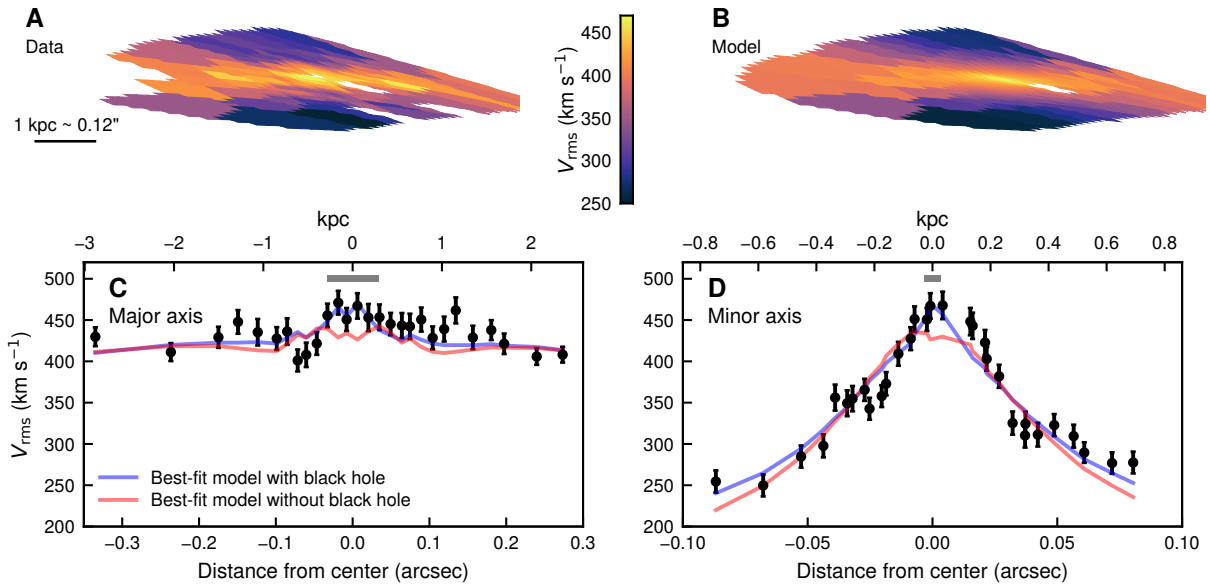


Figure 2: The black hole mass constrained by stellar dynamical models. (A) Source-plane map of the observed projected second velocity moment V_{rms} . (B) V_{rms} map for the best-fit fiducial dynamical model including a black hole. (C) The observed kinematics (black points) in a pseudoslit along the major axis are compared to the best-fit fiducial dynamical model with a black hole (blue curve) and without one (red). The gray rectangle indicates the width of the PSF. (D) Like C but along the minor axis. Models without a black hole cannot match the central V_{rms} peak. Small-scale structure in the model curves is a result of accounting for pixelization and binning.

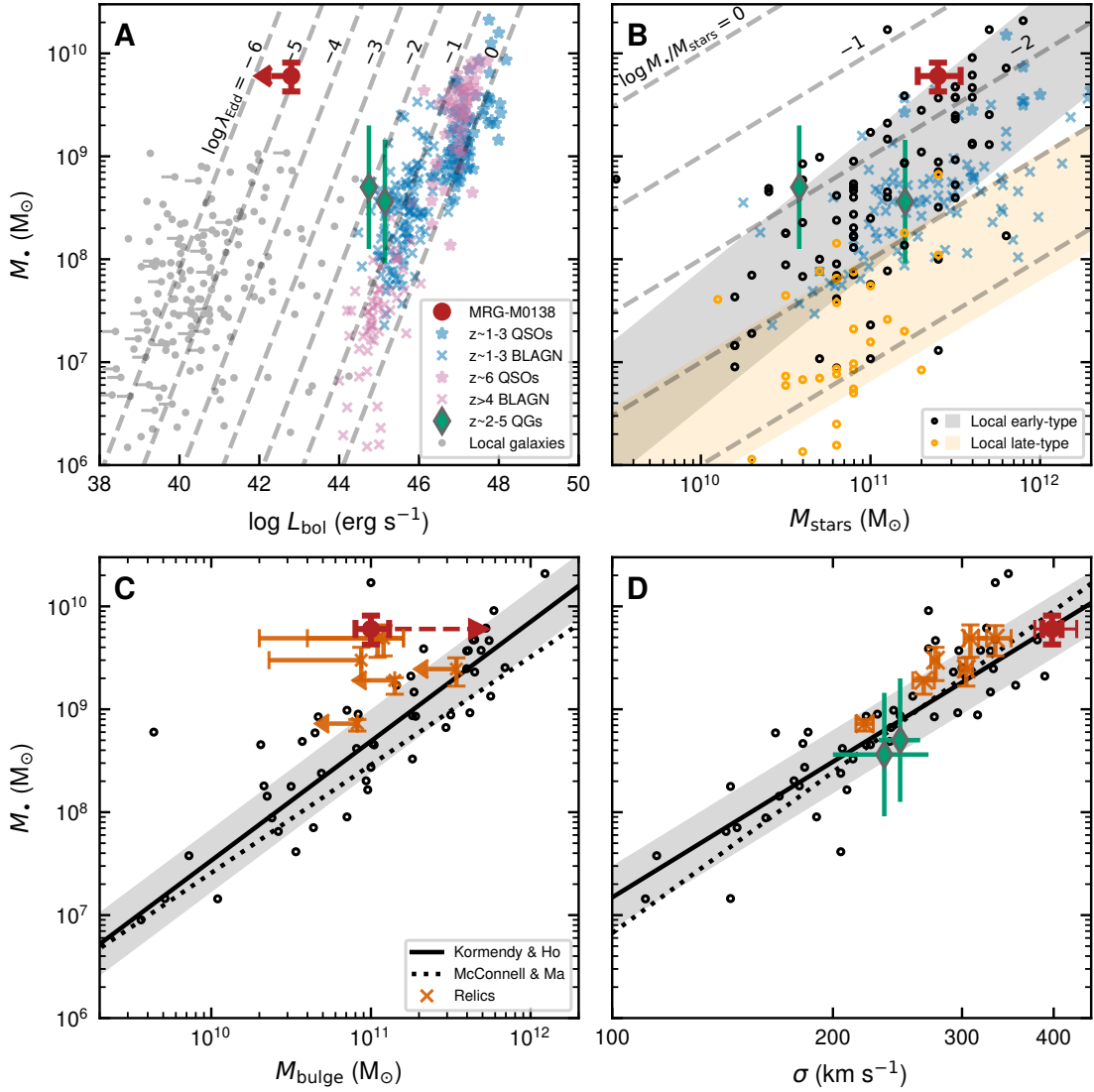


Figure 3: Properties of MRG-M0138 and constraints on the evolution of galaxy–black hole scaling relations. (A) The AGN luminosity and Eddington ratio (diagonal lines) are compared to quasars at $z \sim 1-3$ (55, 56) and $z \sim 6$ (57), broad-line AGN (BLAGN) at $z \sim 1-3$ (19, 33) and $z \geq 4$ (24, 26, 27, 58, 59), two quiescent galaxies (QGs) at $z \sim 2-5$ with BLAGN (31, 32), and the Palomar sample of local galaxies (18). (B) The total stellar mass M_{stars} and the mass ratio M_*/M_{stars} (diagonal lines) are compared to local early- and late-type galaxies with dynamically determined M_* and fitted scaling relations (3), as well as coeval $z \sim 1-3$ samples (symbols follow A, with $z \approx 2-3$ quasars from ref. (60)). (C) The bulge stellar mass M_{bulge} is compared to local early-type galaxies (1) and derived scaling relations (1, 2), along with local relic galaxies (49–54). The dashed line shows the evolution of MRG-M0138 assuming that it transforms into an elliptical and doubles in stellar mass with negligible M_* growth. (D) The velocity dispersion is compared to the samples in C and the $z \sim 2-5$ QGs. Thin error bars on MRG-M0138 show the range of different σ_e definitions (9).

References and Notes

1. J. Kormendy, L. C. Ho, Coevolution (Or Not) of Supermassive Black Holes and Host Galaxies. *ARA&A* **51** (1), 511–653 (2013), doi:10.1146/annurev-astro-082708-101811.
2. N. J. McConnell, C.-P. Ma, Revisiting the Scaling Relations of Black Hole Masses and Host Galaxy Properties. *ApJ* **764** (2), 184 (2013), doi:10.1088/0004-637X/764/2/184.
3. J. E. Greene, J. Strader, L. C. Ho, Intermediate-Mass Black Holes. *ARA&A* **58**, 257–312 (2020), doi:10.1146/annurev-astro-032620-021835.
4. R. Abuter, *et al.*, A dynamical measure of the black hole mass in a quasar 11 billion years ago. *Nature* **627** (8003), 281–285 (2024), doi:10.1038/s41586-024-07053-4.
5. J. E. Greene, L. C. Ho, Estimating Black Hole Masses in Active Galaxies Using the H α Emission Line. *ApJ* **630** (1), 122–129 (2005), doi:10.1086/431897.
6. C. Bertemes, *et al.*, JWST ERS Program Q3D: The pitfalls of virial black hole mass constraints shown for a $z \sim 3$ quasar with an ultramassive host. *A&A* **693**, A176 (2025), doi:10.1051/0004-6361/202450451.
7. K. Mehrgan, *et al.*, A 40 Billion Solar-mass Black Hole in the Extreme Core of Holm 15A, the Central Galaxy of Abell 85. *ApJ* **887** (2), 195 (2019), doi:10.3847/1538-4357/ab5856.
8. A. B. Newman, S. Belli, R. S. Ellis, S. G. Patel, Resolving Quiescent Galaxies at $z \gtrsim 2$. I. Search for Gravitationally Lensed Sources and Characterization of Their Structure, Stellar Populations, and Line Emission. *ApJ* **862** (2), 125 (2018), doi:10.3847/1538-4357/aacd4d.
9. Materials and methods are available as supplementary material.
10. A. B. Newman, S. Belli, R. S. Ellis, Discovery of a Strongly Lensed Massive Quiescent Galaxy at $z = 2.636$: Spatially Resolved Spectroscopy and Indications of Rotation. *ApJ* **813** (1), L7 (2015), doi:10.1088/2041-8205/813/1/L7.
11. S. Toft, *et al.*, A massive, dead disk galaxy in the early Universe. *Nature* **546** (7659), 510–513 (2017), doi:10.1038/nature22388.
12. A. B. Newman, S. Belli, R. S. Ellis, S. G. Patel, Resolving Quiescent Galaxies at $z \gtrsim 2$. II. Direct Measures of Rotational Support. *ApJ* **862** (2), 126 (2018), doi:10.3847/1538-4357/aacd4f.
13. F. D’Eugenio, *et al.*, A fast-rotator post-starburst galaxy quenched by supermassive black-hole feedback at $z = 3$. *Nature Astronomy* (2024), doi:10.1038/s41550-024-02345-1.
14. P. Kroupa, On the variation of the initial mass function. *MNRAS* **322** (2), 231–246 (2001), doi:10.1046/j.1365-8711.2001.04022.x.
15. A. van der Wel, *et al.*, 3D-HST+CANDELS: The Evolution of the Galaxy Size-Mass Distribution since $z = 3$. *ApJ* **788** (1), 28 (2014), doi:10.1088/0004-637X/788/1/28.

16. M. Cappellari, Measuring the inclination and mass-to-light ratio of axisymmetric galaxies via anisotropic Jeans models of stellar kinematics. *MNRAS* **390** (1), 71–86 (2008), doi:10.1111/j.1365-2966.2008.13754.x.
17. S. Thater, *et al.*, Six new supermassive black hole mass determinations from adaptive-optics assisted SINFONI observations. *A&A* **625**, A62 (2019), doi:10.1051/0004-6361/201834808.
18. L. C. Ho, Radiatively Inefficient Accretion in Nearby Galaxies. *ApJ* **699** (1), 626–637 (2009), doi:10.1088/0004-637X/699/1/626.
19. H. Suh, *et al.*, No Significant Evolution of Relations between Black Hole Mass and Galaxy Total Stellar Mass Up to $z \sim 2.5$. *ApJ* **889** (1), 32 (2020), doi:10.3847/1538-4357/ab5f5f.
20. M. Habouzit, *et al.*, Supermassive black holes in cosmological simulations I: $M_{\text{BH}}-M_{\star}$ relation and black hole mass function. *MNRAS* **503** (2), 1940–1975 (2021), doi:10.1093/mnras/stab496.
21. Y. Ni, *et al.*, The Astrid Simulation: Evolution of black holes and galaxies to $z=0.5$ and different evolution pathways for galaxy quenching. arXiv:2409.10666 (2024), doi:10.48550/arXiv.2409.10666.
22. H. Zhang, *et al.*, TRINITY I: self-consistently modelling the dark matter halo-galaxy-supermassive black hole connection from $z = 0-10$. *MNRAS* **518** (2), 2123–2163 (2023), doi:10.1093/mnras/stac2633.
23. A. D. Goulding, *et al.*, UNCOVER: The Growth of the First Massive Black Holes from JWST/NIRSpec-Spectroscopic Redshift Confirmation of an X-Ray Luminous AGN at $z = 10.1$. *ApJ* **955** (1), L24 (2023), doi:10.3847/2041-8213/acf7c5.
24. Y. Harikane, *et al.*, A JWST/NIRSpec First Census of Broad-line AGNs at $z = 4-7$: Detection of 10 Faint AGNs with $M_{\text{BH}} = 10^6 - 10^8 M_{\odot}$ and Their Host Galaxy Properties. *ApJ* **959** (1), 39 (2023), doi:10.3847/1538-4357/ad029e.
25. H. Übler, *et al.*, GA-NIFS: A massive black hole in a low-metallicity AGN at $z \sim 5.55$ revealed by JWST/NIRSpec IFS. *A&A* **677**, A145 (2023), doi:10.1051/0004-6361/202346137.
26. I. Juodžbalis, *et al.*, A dormant overmassive black hole in the early Universe. *Nature* **636** (8043), 594–597 (2024), doi:10.1038/s41586-024-08210-5.
27. R. Maiolino, *et al.*, JADES: The diverse population of infant black holes at $4 < z < 11$: Merging, tiny, poor, but mighty. *A&A* **691**, A145 (2024), doi:10.1051/0004-6361/202347640.
28. M. Yue, *et al.*, EIGER. V. Characterizing the Host Galaxies of Luminous Quasars at $z \gtrsim 6$. *ApJ* **966** (2), 176 (2024), doi:10.3847/1538-4357/ad3914.
29. D. Sijacki, *et al.*, The Illustris simulation: the evolving population of black holes across cosmic time. *MNRAS* **452** (1), 575–596 (2015), doi:10.1093/mnras/stv1340.
30. N. Thomas, R. Davé, D. Anglés-Alcázar, M. Jarvis, Black hole–Galaxy correlations in SIMBA. *MNRAS* **487** (4), 5764–5780 (2019), doi:10.1093/mnras/stz1703.

31. A. C. Carnall, *et al.*, A massive quiescent galaxy at redshift 4.658. *Nature* **619** (7971), 716–719 (2023), doi:10.1038/s41586-023-06158-6.
32. K. Ito, *et al.*, An X-ray-Detected Quiescent Galaxy at $z = 2.09$: Implications for the Connection between AGNs and Galaxy Quenching at High Redshift. arXiv:2408.08492 (2024), doi:10.48550/arXiv.2408.08492.
33. X. Ding, *et al.*, The Mass Relations between Supermassive Black Holes and Their Host Galaxies at $1 < z < 2$ HST-WFC3. *ApJ* **888** (1), 37 (2020), doi:10.3847/1538-4357/ab5b90.
34. Q. Yu, S. Tremaine, Observational constraints on growth of massive black holes. *MNRAS* **335** (4), 965–976 (2002), doi:10.1046/j.1365-8711.2002.05532.x.
35. J. A. Kollmeier, *et al.*, Black Hole Masses and Eddington Ratios at $0.3 < z < 4$. *ApJ* **648** (1), 128–139 (2006), doi:10.1086/505646.
36. F. Fiore, *et al.*, AGN wind scaling relations and the co-evolution of black holes and galaxies. *A&A* **601**, A143 (2017), doi:10.1051/0004-6361/201629478.
37. K. E. Whitaker, *et al.*, Quenching of star formation from a lack of inflowing gas to galaxies. *Nature* **597** (7877), 485–488 (2021), doi:10.1038/s41586-021-03806-7.
38. P. F. Hopkins, L. Hernquist, T. J. Cox, D. Kereš, A Cosmological Framework for the Co-Evolution of Quasars, Supermassive Black Holes, and Elliptical Galaxies. I. Galaxy Mergers and Quasar Activity. *ApJS* **175** (2), 356–389 (2008), doi:10.1086/524362.
39. B. Robertson, *et al.*, A Merger-driven Scenario for Cosmological Disk Galaxy Formation. *ApJ* **645** (2), 986–1000 (2006), doi:10.1086/504412.
40. G. B. Brammer, *et al.*, The Number Density and Mass Density of Star-forming and Quiescent Galaxies at $0.4 \leq z \leq 2.2$. *ApJ* **739** (1), 24 (2011), doi:10.1088/0004-637X/739/1/24.
41. E. Emsellem, *et al.*, The ATLAS^{3D} project - III. A census of the stellar angular momentum within the effective radius of early-type galaxies: unveiling the distribution of fast and slow rotators. *MNRAS* **414** (2), 888–912 (2011), doi:10.1111/j.1365-2966.2011.18496.x.
42. A. Küller, J. P. Ostriker, P. Natarajan, C. N. Lackner, R. Cen, Understanding Black Hole Mass Assembly via Accretion and Mergers at Late Times in Cosmological Simulations. *ApJ* **799** (2), 178 (2015), doi:10.1088/0004-637X/799/2/178.
43. M. Hilz, *et al.*, Relaxation and stripping - The evolution of sizes, dispersions and dark matter fractions in major and minor mergers of elliptical galaxies. *MNRAS* **425** (4), 3119–3136 (2012), doi:10.1111/j.1365-2966.2012.21541.x.
44. L. J. Oldham, M. W. Auger, Galaxy structure from multiple tracers - II. M87 from parsec to megaparsec scales. *MNRAS* **457** (1), 421–439 (2016), doi:10.1093/mnras/stv2982.
45. Event Horizon Telescope Collaboration, *et al.*, First M87 Event Horizon Telescope Results. I. The Shadow of the Supermassive Black Hole. *ApJ* **875** (1), L1 (2019), doi:10.3847/2041-8213/ab0ec7.

46. I. Trujillo, A. Ferré-Mateu, M. Balcells, A. Vazdekis, P. Sánchez-Blázquez, NGC 1277: A Massive Compact Relic Galaxy in the Nearby Universe. *ApJ* **780** (2), L20 (2014), doi:10.1088/2041-8205/780/2/L20.
47. A. Yıldırım, *et al.*, MRK 1216 and NGC 1277 - an orbit-based dynamical analysis of compact, high-velocity dispersion galaxies. *MNRAS* **452** (2), 1792–1816 (2015), doi:10.1093/mnras/stv1381.
48. A. Ferré-Mateu, *et al.*, Two new confirmed massive relic galaxies: red nuggets in the present-day Universe. *MNRAS* **467** (2), 1929–1939 (2017), doi:10.1093/mnras/stx171.
49. J. L. Walsh, *et al.*, The Black Hole in the Compact, High-dispersion Galaxy NGC 1271. *ApJ* **808** (2), 183 (2015), doi:10.1088/0004-637X/808/2/183.
50. J. L. Walsh, *et al.*, A $5 \times 10^9 M_{\odot}$ Black Hole in NGC 1277 from Adaptive Optics Spectroscopy. *ApJ* **817** (1), 2 (2016), doi:10.3847/0004-637X/817/1/2.
51. J. L. Walsh, *et al.*, A Black Hole Mass Determination for the Compact Galaxy Mrk 1216. *ApJ* **835** (2), 208 (2017), doi:10.3847/1538-4357/835/2/208.
52. J. H. Cohn, *et al.*, An ALMA Gas-dynamical Mass Measurement of the Supermassive Black Hole in the Local Compact Galaxy UGC 2698. *ApJ* **919** (2), 77 (2021), doi:10.3847/1538-4357/ac0f78.
53. J. H. Cohn, *et al.*, ALMA Gas-dynamical Mass Measurement of the Supermassive Black Hole in the Red Nugget Relic Galaxy PGC 11179. *ApJ* **958** (2), 186 (2023), doi:10.3847/1538-4357/ad029d.
54. J. H. Cohn, *et al.*, Modeling ALMA Observations of the Warped Molecular Gas Disk in the Red Nugget Relic Galaxy NGC 384. *ApJ* **975** (2), 179 (2024), doi:10.3847/1538-4357/ad7bb0.
55. Y. Shen, Rest-frame Optical Properties of Luminous $1.5 < z < 3.5$ Quasars: The H β -[O III] Region. *ApJ* **817** (1), 55 (2016), doi:10.3847/0004-637X/817/1/55.
56. M. Bischetti, *et al.*, The WISSH quasars project. I. Powerful ionised outflows in hyperluminous quasars. *A&A* **598**, A122 (2017), doi:10.1051/0004-6361/201629301.
57. Y. Shen, *et al.*, Gemini GNIRS Near-infrared Spectroscopy of 50 Quasars at $z \gtrsim 5.7$. *ApJ* **873** (1), 35 (2019), doi:10.3847/1538-4357/ab03d9.
58. J. E. Greene, *et al.*, UNCOVER Spectroscopy Confirms the Surprising Ubiquity of Active Galactic Nuclei in Red Sources at $z > 5$. *ApJ* **964** (1), 39 (2024), doi:10.3847/1538-4357/ad1e5f.
59. J. Matthee, *et al.*, Little Red Dots: An Abundant Population of Faint Active Galactic Nuclei at $z \sim 5$ Revealed by the EIGER and FRESCO JWST Surveys. *ApJ* **963** (2), 129 (2024), doi:10.3847/1538-4357/ad2345.

60. R. Decarli, *et al.*, The quasar $M_{\text{BH}}-M_{\text{host}}$ relation through cosmic time - II. Evidence for evolution from $z = 3$ to the present age. *MNRAS* **402** (4), 2453–2461 (2010), doi:10.1111/j.1365-2966.2009.16049.x.
61. A. B. Newman, MRG-M0138 Observations, Barbara A. Mikulski Archive for Space Telescopes (MAST) (2025), doi:10.17909/ryaj-k740.
62. A. B. Newman, Stellar kinematic data, Dryad (to be published upon acceptance) (2025).
63. J. D. R. Pierel, *et al.*, Lensed Type Ia Supernova “Encore” at $z = 2$: The First Instance of Two Multiply Imaged Supernovae in the Same Host Galaxy. *ApJ* **967** (2), L37 (2024), doi:10.3847/2041-8213/ad4648.
64. E. F. Schlafly, D. P. Finkbeiner, Measuring Reddening with Sloan Digital Sky Survey Stellar Spectra and Recalibrating SFD. *ApJ* **737** (2), 103 (2011), doi:10.1088/0004-637X/737/2/103.
65. M. Cappellari, Full spectrum fitting with photometry in PPXF: stellar population versus dynamical masses, non-parametric star formation history and metallicity for 3200 LEGA-C galaxies at redshift $z \approx 0.8$. *MNRAS* **526** (3), 3273–3300 (2023), doi:10.1093/mnras/stad2597.
66. M. V. Maseda, *et al.*, JWST/NIRSpec Measurements of Extremely Low Metallicities in High Equivalent Width Ly α Emitters. *ApJ* **956** (1), 11 (2023), doi:10.3847/1538-4357/acf12b.
67. M. Cappellari, Y. Copin, Adaptive spatial binning of integral-field spectroscopic data using Voronoi tessellations. *MNRAS* **342** (2), 345–354 (2003), doi:10.1046/j.1365-8711.2003.06541.x.
68. M. Cappellari, vorbin version 3.1.5, <https://pypi.org/project/vorbin/3.1.5/>.
69. M. Cappellari, E. Emsellem, Parametric Recovery of Line-of-Sight Velocity Distributions from Absorption-Line Spectra of Galaxies via Penalized Likelihood. *PASP* **116** (816), 138–147 (2004), doi:10.1086/381875.
70. M. Cappellari, Efficient solution of the anisotropic spherically aligned axisymmetric Jeans equations of stellar hydrodynamics for galactic dynamics. *MNRAS* **494** (4), 4819–4837 (2020), doi:10.1093/mnras/staa959.
71. M. Cappellari, ppxf version 9.1.1, <https://pypi.org/project/ppxf/9.1.1/>.
72. A. Vazdekis, M. Koleva, E. Ricciardelli, B. Röck, J. Falcón-Barroso, UV-extended E-MILES stellar population models: young components in massive early-type galaxies. *MNRAS* **463** (4), 3409–3436 (2016), doi:10.1093/mnras/stw2231.
73. M. Jafariyazani, *et al.*, Resolved Multi-element Stellar Chemical Abundances in the Brightest Quiescent Galaxy at $z \sim 2$. *ApJ* **897** (2), L42 (2020), doi:10.3847/2041-8213/aba11c.
74. Space Telescope Science Institute, JWST User Documentation (JDox) (2016-2025), <https://jwst-docs.stsci.edu>.

75. M. Kriek, C. Conroy, The Dust Attenuation Law in Distant Galaxies: Evidence for Variation with Spectral Type. *ApJ* **775** (1), L16 (2013), doi:10.1088/2041-8205/775/1/L16.
76. C. Spiniello, S. Trager, L. V. E. Koopmans, C. Conroy, The stellar IMF in early-type galaxies from a non-degenerate set of optical line indices. *MNRAS* **438** (2), 1483–1499 (2014), doi: 10.1093/mnras/stt2282.
77. C. Conroy, J. E. Gunn, M. White, The Propagation of Uncertainties in Stellar Population Synthesis Modeling. I. The Relevance of Uncertain Aspects of Stellar Evolution and the Initial Mass Function to the Derived Physical Properties of Galaxies. *ApJ* **699** (1), 486–506 (2009), doi:10.1088/0004-637X/699/1/486.
78. C. Conroy, J. E. Gunn, The Propagation of Uncertainties in Stellar Population Synthesis Modeling. III. Model Calibration, Comparison, and Evaluation. *ApJ* **712** (2), 833–857 (2010), doi:10.1088/0004-637X/712/2/833.
79. S. Ertl, *et al.*, Cosmology with Supernova Encore in the strong lensing cluster MACS J0138–2155: photometry, cluster members, and lens mass model. arXiv:2503.09718 (2025).
80. S. A. Rodney, *et al.*, A gravitationally lensed supernova with an observable two-decade time delay. *Nature Astronomy* **5**, 1118–1125 (2021), doi:10.1038/s41550-021-01450-9.
81. M. Cappellari, Efficient multi-Gaussian expansion of galaxies. *MNRAS* **333** (2), 400–410 (2002), doi:10.1046/j.1365-8711.2002.05412.x.
82. M. Cappellari, mgefit version 5.0.15, <https://pypi.org/project/mgefit/5.0.15/>.
83. G. A. D. Savorgnan, A. W. Graham, Explaining the reportedly overmassive black holes in early-type galaxies with intermediate-scale discs. *MNRAS* **457** (1), 320–327 (2016), doi: 10.1093/mnras/stv2713.
84. M. Cappellari, jampy version 8.0.0, <https://pypi.org/project/jampy/8.0.0/>.
85. B. Wang, M. Cappellari, Y. Peng, Physical explanation for the galaxy distribution on the (λ_R , ϵ) and (V/σ , ϵ) diagrams or for the limit on orbital anisotropy. *MNRAS* **500** (1), L27–L31 (2021), doi:10.1093/mnrasl/slaa176.
86. C. Conroy, P. G. van Dokkum, A. Villaume, The Stellar Initial Mass Function in Early-type Galaxies from Absorption Line Spectroscopy. IV. A Super-Salpeter IMF in the Center of NGC 1407 from Non-parametric Models. *ApJ* **837** (2), 166 (2017), doi:10.3847/1538-4357/aa6190.
87. P. van Dokkum, C. Conroy, A. Villaume, J. Brodie, A. J. Romanowsky, The Stellar Initial Mass Function in Early-type Galaxies from Absorption Line Spectroscopy. III. Radial Gradients. *ApJ* **841** (2), 68 (2017), doi:10.3847/1538-4357/aa7135.
88. K. Mehrgan, *et al.*, Dynamical Stellar Mass-to-light Ratio Gradients: Evidence for Very Centrally Concentrated IMF Variations in ETGs? *ApJ* **961** (1), 127 (2024), doi:10.3847/1538-4357/acfe09.

89. S. Posacki, M. Cappellari, T. Treu, S. Pellegrini, L. Ciotti, The stellar initial mass function of early-type galaxies from low to high stellar velocity dispersion: homogeneous analysis of ATLAS^{3D} and Sloan Lens ACS galaxies. *MNRAS* **446** (1), 493–509 (2015), doi:10.1093/mnras/stu2098.
90. Planck Collaboration, *et al.*, Planck 2015 results. XIII. Cosmological parameters. *A&A* **594**, A13 (2016), doi:10.1051/0004-6361/201525830.
91. J. Buchner, UltraNest - a robust, general purpose Bayesian inference engine. *The Journal of Open Source Software* **6** (60), 3001 (2021), doi:10.21105/joss.03001.
92. J. Buchner, UltraNest version 4.3.3, <https://johannesbuchner.github.io/UltraNest/index.html>.
93. L. C. Ho, A. V. Filippenko, W. L. W. Sargent, A Search for “Dwarf” Seyfert Nuclei. VI. Properties of Emission-Line Nuclei in Nearby Galaxies. *ApJ* **583** (1), 159–177 (2003), doi:10.1086/345354.
94. A. Fruscione, *et al.*, CIAO: Chandra’s data analysis system, in *Observatory Operations: Strategies, Processes, and Systems*, D. R. Silva, R. E. Doxsey, Eds., vol. 6270 of *Society of Photo-Optical Instrumentation Engineers (SPIE) Conference Series* (2006), p. 62701V, doi:10.1117/12.671760.
95. Chandra X-Ray Center, CIAO version 4.17, <https://cxc.cfa.harvard.edu/ciao4.17/>.
96. Y. Shen, *et al.*, A Catalog of Quasar Properties from Sloan Digital Sky Survey Data Release 7. *ApJS* **194** (2), 45 (2011), doi:10.1088/0067-0049/194/2/45.
97. A. Bongiorno, *et al.*, The $M_{\text{BH}}-M_*$ relation for X-ray-obscured, red QSOs at $1.2 < z < 2.6$. *MNRAS* **443** (3), 2077–2091 (2014), doi:10.1093/mnras/stu1248.
98. M. Vestergaard, B. M. Peterson, Determining Central Black Hole Masses in Distant Active Galaxies and Quasars. II. Improved Optical and UV Scaling Relationships. *ApJ* **641** (2), 689–709 (2006), doi:10.1086/500572.
99. M. B. Bagley, *et al.*, CEERS Epoch 1 NIRCcam Imaging: Reduction Methods and Simulations Enabling Early JWST Science Results. *ApJ* **946** (1), L12 (2023), doi:10.3847/2041-8213/acbb08.
100. Gaia Collaboration, *et al.*, Gaia Data Release 3. Summary of the content and survey properties. *A&A* **674**, A1 (2023), doi:10.1051/0004-6361/202243940.
101. L. Bradley, astropy/photutils: 1.8.0 (2023), doi:10.5281/zenodo.7946442, <https://doi.org/10.5281/zenodo.7946442>.
102. D. R. Law, *et al.*, A 3D Drizzle Algorithm for JWST and Practical Application to the MIRI Medium Resolution Spectrometer. *AJ* **166** (2), 45 (2023), doi:10.3847/1538-3881/acdddcc.
103. P. Virtanen, *et al.*, SciPy 1.0: Fundamental Algorithms for Scientific Computing in Python. *Nature Methods* **17**, 261–272 (2020), doi:10.1038/s41592-019-0686-2.

104. SciPy version 1.7.3, <https://pypi.org/project/scipy/1.7.3/>.

Acknowledgments

Funding: This work is based on observations made with the NASA/ESA/CSA James Webb Space Telescope. These observations are associated with programs GO-2345 and DD-6549. Support for programs GO-2345 and DD-6549 was provided by NASA through a grant from the Space Telescope Science Institute, which is operated by the Association of Universities for Research in Astronomy, Inc., under NASA contract NAS 5-03127. The data were obtained from the Mikulski Archive for Space Telescopes at the Space Telescope Science Institute. This research has made use of data obtained from the Chandra Data Archive provided by the Chandra X-ray Center (CXC). A.B.N. performed part of this work at the Aspen Center for Physics, which is supported by National Science Foundation grant PHY-2210452. A.Z. acknowledges support by Grant No. 2020750 from the United States–Israel Binational Science Foundation (BSF) and Grant No. 2109066 from the United States National Science Foundation (NSF); and by the Israel Science Foundation Grant No. 864/23. S.B. acknowledges funding from NASA ATP 80NSSC22K1897. R.S.E. acknowledges financial support from the Peter and Patricia Gruber Foundation. M.J.J. acknowledges support for the current research from the National Research Foundation (NRF) of Korea under the programs 2022R1A2C1003130 and RS-2023-00219959. S.S. has received funding from the European Union’s Horizon 2022 research and innovation programme under the Marie Skłodowska-Curie grant agreement No 101105167 — FASTIDIoUS. This work was supported by JSPS KAKENHI Grant Numbers JP22K21349, JP23K13149. S.C. acknowledges that this research was supported by Basic Science Research Program through the National Research Foundation of Korea (NRF) funded by the Ministry of Education (No. RS-2024-00413036). A.A. acknowledges financial support through the Beatriz Galindo programme and the project PID2022-138896NB-C51 (MCIU/AEI/MINECO/FEDER, UE), Ministerio de Ciencia, Investigación y Universidades. S.E. and S.H.S. thank the Max Planck Society for support through the Max Planck Fellowship for S.H.S. This project has received funding from the European Research Council (ERC) under the European Union’s Horizon 2020 research and innovation programme (LENSNOVA: grant agreement No 771776). This work is supported in part by the Deutsche Forschungsgemeinschaft (DFG, German Research Foundation) under Germany’s Excellence Strategy – EXC-2094 – 390783311. G.G. acknowledges financial support through grant PRIN-MIUR 2020SKSTHZ. C.G., P.B., and P.R. acknowledge support through grant MIUR2020 SKSTHZ. J.E.G. acknowledges support from NSF AAG grant 2306950. S.B. is supported by the ERC Starting Grant ‘Red Cardinal’, GA 101076080. J.L.W. acknowledges the support of NSF AST-2206219. K.G. and T.N. acknowledge support from Australian Research Council Laureate Fellowship FL180100060. K.G. and T.M.B. acknowledge support from Australian Research Council Discovery Project DP230101775.

Author contributions: A.B.N. led the analysis of the source kinematics, stellar populations, and structure; the dynamical modeling; and the writing of the paper. M.G. reduced the spectroscopic data. S.G. mapped the gas absorption. A.M. searched for archival data. A.B.N., S.B., R.S.E., K.G., M.J., M.K., T.N., and J.P. contributed to the acquisition, planning, and execution of the observations. S.B. and A.B.N. performed the ASTRID comparison. S.H.S., S.E., G.C., G.G., C.G., and S.S. constructed the fiducial lens model. A.A., P.B., S.C., J.M.D., N.F., B.F., Y.F., M.J.J., P.S.K.,

A.K.M., S.N., M.O., P.R., and A.Z. constructed the other lens models. A.M.K. performed the data reduction used in the lens modeling. All authors contributed to the interpretation of the results and to the writing of the paper.

Competing interests: There are no competing interests to declare.

Data and materials availability: Observations analyzed in this work are available from the Barbara A. Mikulski Archive for Space Telescopes (MAST) (61). Measurements of the stellar kinematics and associated data, including the PSF and source plane coordinates, are available from (62).

Supplementary materials

Materials and Methods

Supplementary Text

Figs. S1 to S8

Tables S1 to S2

Supplementary Materials for A stellar dynamical mass measure of an inactive black hole in the distant universe

Andrew B. Newman*, Meng Gu, Sirio Belli, Richard S. Ellis, Sai Gangula, Jenny E. Greene,
Jonelle L. Walsh, Sherry H. Suyu, Sebastian Ertl, Gabriel Caminha, Giovanni Granata,
Claudio Grillo, Stefan Schuldt, Tania M. Barone, Simeon Bird, Karl Glazebrook,
Marziye Jafariyazani, Mariska Kriek, Allison Matthews, Takahiro Morishita,
Themiyā Nanayakkara, Justin D. R. Pierel, Ana Acebrón, Pietro Bergamini, Sangjun Cha,
Jose M. Diego, Nicholas Foo, Brenda Frye, Yoshinobu Fudamoto, M. James Jee,
Patrick S. Kamieneski, Anton M. Koekemoer, Asish K. Meena, Shun Nishida, Masamune Oguri,
Piero Rosati, Adi Zitrin

*Corresponding author. Email: anewman@carnegiescience.edu

This PDF file includes:

Materials and Methods
Supplementary Text
Figures S1 to S8
Tables S1 to S2

Materials and Methods

Observations

Initial images of MRG-M0138 were obtained through the JWST program GO-2345. Following the discovery of supernova (SN) Encore in those images (63), deeper NIRC*am* images were obtained through program DD-6549, which provided 50–77 min of total exposure in each of the F115W, F150W, F200W, F277W, F356W, and F444W filters. We also used an 87 min observation from the Hubble Space Telescope (HST) Advanced Camera for Surveys (ACS) through the F555W filter (GO-14496).

The NIRS*pec* IFU observations (GO-2345) used the G140M/F100LP and G235M/F170LP grating/filter pairs. Since the source emission fills the IFU, we also observed off-source pointings to measure the background radiation. The G235M observation on 2023 Nov 18 used a 4-POINT-DITHER sequence to provide 127 min exposure in each of the on- and off-source fields. The G140M observation on 2023 Dec 27 provided 137 min exposure per field. The reduction of the images and spectra is described in the Supplementary Text, including custom processing steps. The spectra were resampled to data cubes with 0.05'' spaxels.

Preparation of spectra and photometry for modeling

We logarithmically rebinned the G140M and G235M spectra and their variances onto a common wavelength grid with 132 km s⁻¹ per pixel. The two data cubes were shifted to the systemic rest frame ($z_{\text{sys}} = 1.9480$) and spliced together at a transition wavelength of $\lambda_{\text{rest}} = 0.615 \mu\text{m}$. We removed Milky Way extinction (64) from the spectra and images. SPS models (see Stellar population synthesis modeling) were then fit to the spectra in each individual spaxel. These initial fits were used only to iteratively identify outlier pixels ($> 3\sigma$, 0.6% of pixels) and to adjust the pipeline noise spectra (65), which we rescaled by factors of ≈ 1.2 –2.0 to achieve a reduced $\chi^2_{\nu} = 1$; such corrections are common (66). We defined the signal-to-noise ratio (SNR) of a spectrum as the median ratio using these rescaled noise estimates.

We spatially binned the spectra to a target SNR of 40 by applying *vorbin* version 3.1.5 (67, 68) to the 1341 spaxels with a F200W surface brightness exceeding 1.0 MJy sr⁻¹, excluding 10 spaxels contaminated by SN Encore. To account for correlated noise in nearby spaxels, which is substantial due to the resampling, we provided *vorbin* with a custom function to fit SPS models to a binned spectrum and thereby estimate the noise and identify outliers as described above. We arrived at 219 Voronoi bins with SNR = 23–64 (median 42; see Fig. S1) and sizes of 1–68 spaxels, with 129 bins being single spaxels. Within each bin, we derived matched photometry from the average surface brightness of the constituent pixels in each of the 7 images, convolved to match the broadest PSF (F444W, FWHM = 0.147''), which is close to the NIRS*pec* IFU PSF (FWHM = 0.127''; Supplementary Text). Because the errors in the photometry are dominated by small systematics, we increased the random errors by adding, in quadrature, 3% of the maximum F_{λ} (always F150W) in each spatial bin, similar to the approach of ref. (65).

Stellar population synthesis modeling

We used *ppxf* version 9.1.1 to model the spectrophotometry and measure stellar populations and kinematics (65, 69–71). The input SPS models were simple stellar populations from the E-MILES

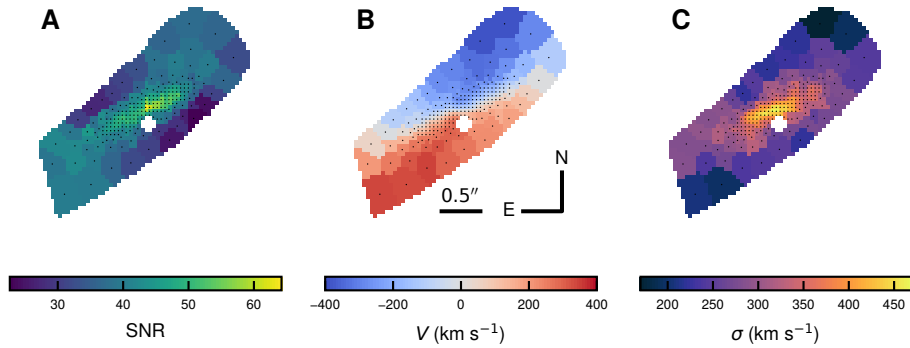


Figure S1: Voronoi binning and image plane stellar kinematics. (A) The SNR of the Voronoi binned spectra. Points show the center of each bin. The white cross south of the center was excluded from the binning due to contamination from SN Encore. (B) The stellar velocity in each bin. (C) The stellar velocity dispersion in each bin.

library (72), which `ppxf` combined with regularized weights to allow for flexible star formation histories. To cover the necessary wavelength range, we restricted the simple stellar populations to ages of 0.14–4 Gyr and metallicities of $[Z/H] = -0.4, 0, \text{ and } 0.22$. These limits are appropriate for MRG-M0138, which is metal-rich (73) and quiescent (8). The upper limit on age permitted stars slightly older than the universe to allow for model uncertainties. The models were built with a Salpeter IMF, but we rescaled all stellar masses by a factor 0.66 so that our SPS-based mass estimates $M_{*,\text{MW}}$ refer to a Milky Way IMF (14). The model spectra were convolved to match the wavelength-dependent instrumental resolution (74). We adopted the default dust attenuation law (75). We further modeled line emission from the hydrogen Balmer series, [O II] $\lambda\lambda 3727, 3730$, [O III] $\lambda\lambda 4960, 5008$, [O I] $\lambda\lambda 6302, 6366$, [N II] $\lambda\lambda 6550, 6585$, and [S II] $\lambda\lambda 6718, 6733$. Since the Balmer emission lines were not detected, we assumed the emission lines are attenuated like the starlight.

We masked $\pm 1500 \text{ km s}^{-1}$ intervals around several features: Na D and Ca K, which may be affected by gas absorption; Mg b, Na I 8190, and TiO2 (76), which are affected by α -enhancement and the IMF and showed significant residuals in some spectra; and transitions at 6150 \AA (G140M to G235M) and 8949 \AA (resolution change in E-MILES). We also masked $\pm 200 \text{ \AA}$ around 7250 \AA due to systematic residuals.

To map the stellar mass-to-light ratio $(M_*/L)_{\text{MW}}$, which we used to model the stellar mass distribution, we simultaneously fit the 7-band photometry and the spectra from $\lambda_{\text{rest}} = 0.36\text{--}1.02 \text{ }\mu\text{m}$. We allowed the models to be modulated by a multiplicative polynomial with order $N_{\text{mult}} = 3$ to mitigate flux calibration errors. In each spatial bin, we measured $(M_*/L)_{\text{MW}}$ in the F200W filter ($\lambda_{\text{rest}} \approx 0.68 \text{ }\mu\text{m}$). Fig. S2 demonstrates the high quality of the data and models.

Stellar kinematics

We measured the stellar V and σ in each binned spectrum largely as described above, with a few differences: we omitted the wavelength range $< 0.40 \text{ }\mu\text{m}$, which reduced the sensitivity of the kinematics to the polynomial orders; we included an additive polynomial with order $N_{\text{add}} = 2$; and

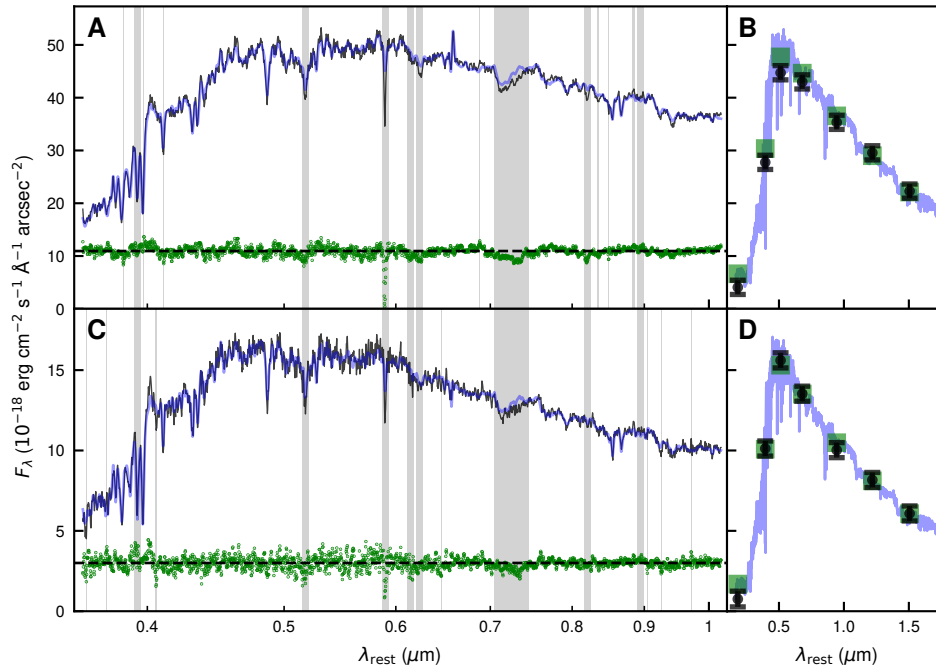


Figure S2: Spectrophotometry and SPS model fits in two spatial bins. (A) The observed spectrum (black) and fitted model (blue) for the central spaxel. Residuals are shown as green points, with the zero point shifted to the dashed line. Grey bands indicate masked pixels: thin bands represent outlier pixels rejected during the fit, and thick bands represent wavelength regions masked for the reasons discussed in the text. (B) The observed photometry (black), model spectrum (blue), and synthesized model photometry (green boxes). (C) and (D) Like A and B, but for the spatial bin with the median SNR.

we omitted the photometry and thus did not model dust attenuation, which was subsumed into the multiplicative polynomial. Fig. S1 shows the kinematic maps in the image plane, and Fig. 1 shows the source plane (see Lens models, below).

We estimated the random errors in V and σ by comparing measurements derived from the G140M and G235M spectra separately. We computed a reduced $\chi^2_v = 1.9\text{--}2.1$ for the G140M–G235M differences in V and σ , using the formal errors returned by `ppxf`. We therefore increased these errors by a factor of 1.4, resulting in median 1σ uncertainties in V and σ of 10 km s^{-1} and 13 km s^{-1} , respectively.

Systematic uncertainties in σ were evaluated by varying several analysis choices and measuring changes to the median σ over the 30 highest-SNR bins. First, we varied the polynomial orders over $0 \leq N_{\text{mult}} \leq 6$ and $-1 \leq N_{\text{add}} \leq 6$, where -1 indicates no polynomial. The results were remarkably stable: provided that $N_{\text{mult}} \geq 2$ and $N_{\text{add}} \geq 0$, systematic changes to σ were $\lesssim 1\%$. Second, we extracted kinematics from narrow $0.1\ \mu\text{m}$ -wide chunks to evaluate the sensitivity to wavelength. For this test we fixed the template to the one determined from the full spectral range, and we used low-order polynomials ($N_{\text{mult}} = 1$ and $N_{\text{add}} = -1$) given the narrow wavelength range being fit. Excepting the $0.7\text{--}0.8\ \mu\text{m}$ interval, which is largely masked, we found that the median σ varied by $\pm 2.7\%$ (rms). Third, we found that σ measurements derived using the stellar population settings in the previous section were lower by 2% . Fourth, we extracted kinematics using FSPS templates (77, 78) and found no systematic shift. Altogether we estimated a systematic uncertainty of 3% in σ .

MRG-M0138 is globally dust-poor (37), yet our SPS modeling indicates some regions with modest attenuation, including near the center (Fig. S3B). To test whether dust affects the observed line-of-sight kinematics, we compared our fiducial kinematic measures to a second set derived by fitting only the reddest part of the spectrum at $\lambda_{\text{rest}} > 0.8\ \mu\text{m}$, including the calcium triplet. In the inner galaxy, we found no systematic differences or increased scatter between the two V_{rms} measures for the vast majority of bins with $A_V < 0.3\text{ mag}$ (Fig. S3). This indicates that dust generally has a minimal effect on the observed kinematics. The 3 inner bins with $A_V = 0.3\text{--}0.34\text{ mag}$ (indicated by crosses in Fig. S3B-C) do show possible dust effects, and we therefore masked them for our dynamical modeling, along with 2 additional bins with $A_V > 0.3\text{ mag}$ at larger radius.

Lens models

Our analysis relies on a lens model constrained by the positions of 23 images of 8 sources with 4 different spectroscopic redshifts. Specifically, we used the `iso_halo` model of ref. (79), which we refer to as the fiducial lens model. Systematic uncertainties, which are typically dominant, were evaluated by comparing results from seven lens modeling groups who employed a wide variety of modeling methods. We compared μ estimates near the center of the JWST-targeted image (image 2, as labeled by (8)), using each team’s “ultimate” model based on the most secure set of “gold” multiple images (79). These μ estimates range from $\Delta\mu/\mu_{\text{fid}} = -39\%$ to $+44\%$ relative to the fiducial model, i.e., $\mu = 29^{+13}_{-11}$. The lens models differ mainly in the total magnification μ ; differences in the ratio of the tangential to radial magnification, which affects the source ellipticity, are small enough to have a comparatively negligible influence on M_\bullet . We note that although previous lens models indicated lower magnifications (8, 80), they were based on many fewer constraints.

We quote the spatial resolution of the observations at the center of MRG-M0138 (image 2) by casting PSFs to the source plane using the fiducial lens model and fitting an anisotropic 2D

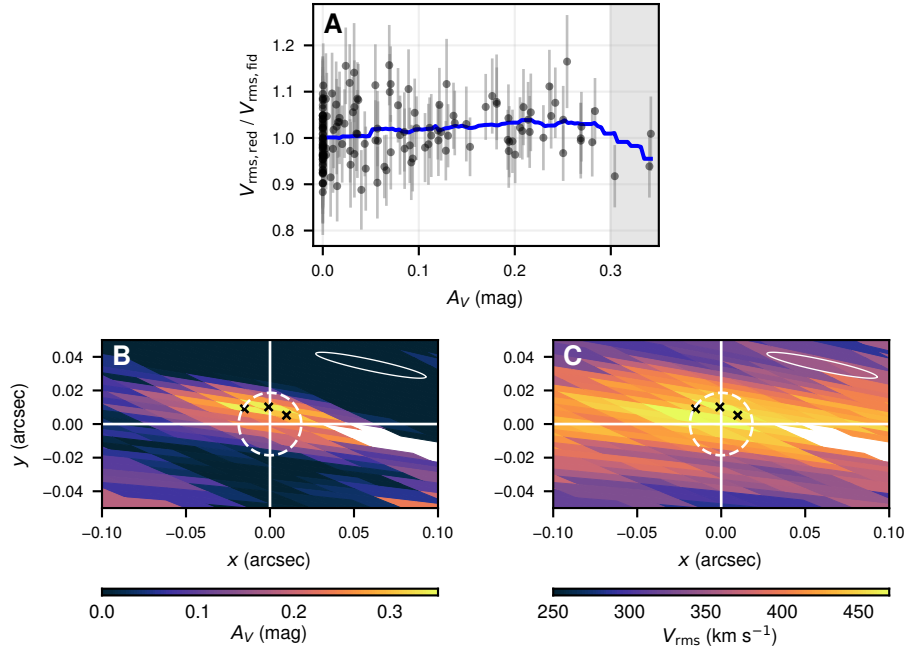


Figure S3: Tests of the influence of dust on the inner stellar kinematics. (A) The ratio of V_{rms} , as measured using only the red portion of the spectrum ($\lambda_{\text{rest}} > 0.8 \mu\text{m}$), to the fiducial value, as a function of A_V for spaxels within $0.1''$ (source plane) of the galaxy center. The blue line is a running mean and shows evidence of systematic wavelength-dependent differences only in a few spaxels with $A_V > 0.3$ mag. (B) Source-plane map of the dust extinction in the inner region as derived from SPS modeling. Crosses show the bins masked in the dynamical modeling due to high A_V . The PSF is shown in the upper right corner. The radius of the dashed circle is r_{inf} . x and y are aligned with major and minor axes, respectively. (C) Like B but mapping V_{rms} .

Gaussian. The NIRCam F200W and NIRSpc IFU PSFs have source-plane sizes of $\sigma = 1.9 \text{ mas} \times 17 \text{ mas}$ ($16 \times 149 \text{ pc}$) and $\sigma = 3.4 \text{ mas} \times 34 \text{ mas}$ ($29 \times 288 \text{ pc}$), respectively, elongated 12° from the major axis. The effective resolution is the geometric mean of the two dimensions, $\sigma_{\text{psf}} = 5.7 \text{ mas} = 49 \text{ pc}$ (F200W) and $11 \text{ mas} = 91 \text{ pc}$ (IFU).

Stellar light and mass distributions

We modeled the distributions of stellar light and mass using multi-Gaussian expansions (MGEs) (41), as required by JAM. The light map was computed by multiplying the F200W image by a factor $4802 L_\odot \text{ pc}^{-2} (\text{MJy sr}^{-1})^{-1}$. Like the $(M_*/L)_{\text{MW}}$ calculation, L_\odot was evaluated through the F200W filter bandpass shifted by a factor $(1 + z_{\text{sys}})^{-1}$. We defined the center as the surface brightness peak, after light smoothing, and found it to exhibit a dispersion of only 1 mas (source plane) among the NIRCam images, which demonstrates its insensitivity to dust. To identify dusty regions to exclude from the fit, we constructed a F115W–F200W color map (Fig. S4A-B). By examining this map and residuals from initial MGE models, we identified two dusty regions located above the center and in the lower-right part of the disk (red in Fig. S4). We also masked the vicinity of SN Encore (green).

We fit an initial model to the F200W image, resampled to the source plane, using `mgefit` (81, 82). We used the bulge-disk mode, which greatly simplifies the treatment of possible IMF gradients in our dynamical models. We then refined this initial `mgefit` model by fitting in the image plane (Supplementary Text), which is necessary to properly account for the PSF. Figs. S4C-D show that the resulting MGE model provided a good description of the galaxy structure. We note that the apparent isophote twist near the center is produced by the anisotropy of the PSF in the source plane and is not intrinsic to the model, which is axisymmetric. The largest residuals are close to the major axis at $x \approx -0.4$ (Fig. S4C). The excess light here seems to reflect an actual asymmetry in part of the outer disk. In our dynamical models, we also found elevated residuals in this region and therefore masked 2 spatial bins.

Dynamical modeling also requires the distribution of stellar mass. Our SPS modeling provided an estimate of $(M_*/L)_{\text{MW}}$ for each binned spectrum. To transfer these estimates onto the higher-resolution NIRCcam images, we fit a linear relation $(M_*/L)_{\text{MW}}/(M_*/L)_\odot = 0.80 \times (\text{F115W} - \text{F200W}) - 0.26$. The fitted range is $\approx 0.7 - 1.1 (M/L)_\odot$. We used this relation to construct a map of the stellar mass surface density, to which we then fit an MGE model using the same methods described above (Fig. S4E-F). The MGE components of the light and stellar mass models are listed in Table S1. We emphasize that this procedure provides a fiducial stellar mass distribution from which our dynamical modeling ultimately allows large deviations.

Galaxy structural and kinematic properties

R_e measurements were derived from the F200W MGE model using the `mge_half_light_isophote` routine (82). Errors on all masses ($M_{*,\text{MW}}$, M_{bulge} , M_{stars}) and R_e include the magnification uncertainty. Local relic galaxies often exhibit a decline in ellipticity at large radii $R_{\text{maj}} \gtrsim 5 - 10 \text{ kpc}$, as a round outer envelope begins to dominate over the disk, and the decision of whether to include this envelope in the bulge mass is a significant source of disagreement (47, 83). We found no clear evidence of a declining ellipticity in the outer parts of MRG-M0138 to a limiting $R_{\text{maj}} \sim 12 \text{ kpc}$, and thus we did not attempt to model any additional component.

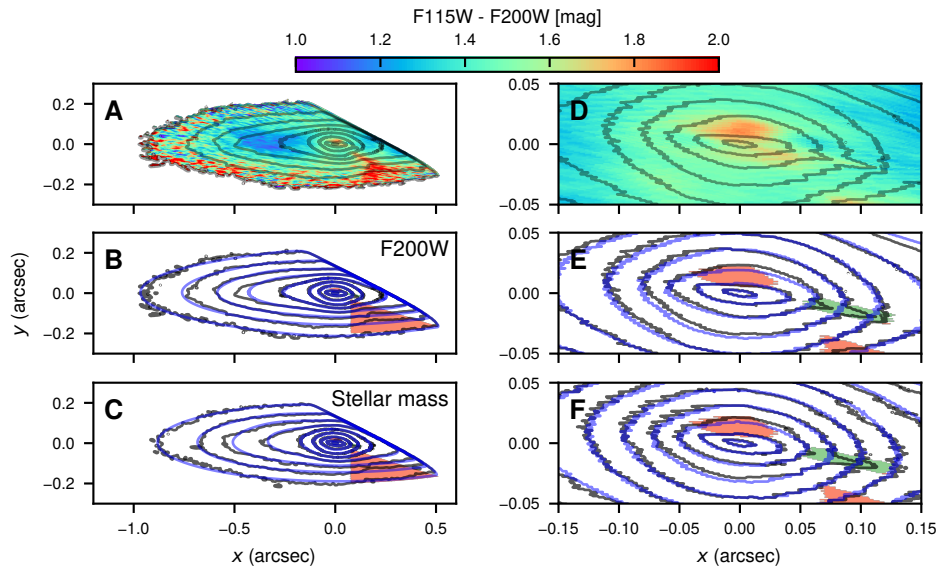


Figure S4: Models of the stellar light and mass distributions. (A) Source-plane map of the F115W–F200W color with F200W isophotes overlaid, spaced by 0.3 dex in surface brightness. (B) Observed F200W isophotes (black), as in A, and the MGE model (blue). Red and green regions are masked due to dust and SN Encore, respectively. (C) Like B, but showing the stellar mass surface density, as estimated using the color– M_*/L relation derived from the SPS models. (D), (E), and (F) Like A, B, and C, respectively, but zoomed into the central region and showing isophotes spaced by 0.2 dex.

We defined σ_e^2 as the intensity-weighted V_{rms}^2 within apertures corresponding to 3 different conventions: (1) the half-light ellipse of the entire system, $\sigma_e = 377 \pm 11 \text{ km s}^{-1}$, (2) the half-light ellipse of the bulge, $\sigma_e = 398 \pm 12 \text{ km s}^{-1}$, and (3) a narrow major-axis slit extending to the total half-light radius, $\sigma_e = 430 \pm 13 \text{ km s}^{-1}$. These errors reflect the 3% systematic uncertainty. We did not exclude the sphere of influence (2) but found that doing so would have a small effect ($\lesssim 8 \text{ km s}^{-1}$). We used definition 2 to compute $r_{\text{inf}} = GM_{\bullet}/\sigma_e^2 = 164 \text{ pc}$ and to plot MRG-M0138 in Fig. 3, where the thin error bars indicate the range of definitions 1–3.

Dynamical models

We built a range of dynamical models using `jumpy` version 8.0.0 (16, 70, 84). The code calculates stellar dynamics within an axisymmetric system in which the luminosity and mass distributions are specified as MGEs. It assumes that the velocity ellipsoid is aligned with either cylindrical (cyl) or spherical (sph) coordinates; our models include both possibilities. All models included parameters for (1) inclination i ; (2) black hole mass M_{\bullet} ; (3) a gradient in the velocity anisotropy β_z (cyl) or β_r (sph) given by the logistic profile that `jumpy` provides, which is specified by the inner and outer values, β_0 and β_{∞} , and a transition height z_{β} (cyl) or radius r_{β} (sph); and (4) a spherical power-law dark matter halo specified by a slope γ_{DM} , where $\rho_{\text{DM}} \propto r^{-\gamma_{\text{DM}}}$, and the dark matter fraction f_{DM} within a 5-kpc sphere. We fixed `alpha`, the `jumpy` parameter that controls the speed of the transition from β_0 to β_{∞} , to 2 and verified that our analysis is insensitive to this choice. (This `jumpy` parameter is unrelated to our α , defined below.) Based on initial fits, the systemic velocity was fixed to $v_{\text{sys}} = 1 \text{ km s}^{-1}$ relative to $z = 1.9480$.

Our stellar mass surface density map accounts for spatial gradients in age, metallicity, and dust. We introduced additional flexibility into the dynamical models to allow for uncertainties in the SPS models and for the possibility of a non-Milky Way IMF. Specifically, we defined a parameter $\alpha = (M_*/L)/(M_*/L)_{\text{MW}}$ that rescales the SPS-based estimate $(M_*/L)_{\text{MW}}$, and we further allowed α to vary spatially. Because the manner of spatial variation is unknown *a priori*, we considered several models:

Model A: The bulge and disk stars have their own α values, α_{bulge} and α_{disk} , which are spatially constant within each.

Model B: The bulge and disk stars participate in a common radial gradient, in which α follows a logistic profile in $\log r$, a form that avoids unphysical values:

$$\alpha(r) = \alpha_0 + \frac{\alpha_{\infty} - \alpha_0}{1 + e^{-x}} \quad \text{with} \quad x = -2 + 4 \frac{\log r / r_{\alpha}^{\text{in}}}{\log r_{\alpha}^{\text{out}} / r_{\alpha}^{\text{in}}}. \quad (\text{S1})$$

Thus $\alpha(r) \approx \alpha_0$ at small $r \ll r_{\alpha}^{\text{in}}$, $\alpha(r) \approx \alpha_{\infty}$ at large $r \gg r_{\alpha}^{\text{out}}$, and $\alpha(r)$ transitions between these values over intermediate radii. We defined r_{α}^{in} and r_{α}^{out} such that the transition is $(1 + e^{-2})^{-1} \approx 88\%$ complete at these radii. To impose a gradient on the stellar mass MGE model, we first evaluated the stellar mass density profile $\rho_*(r)$ of the disk MGE components in the equatorial plane. We then multiplied this profile by $\alpha(r)$ and solved for a new one-dimensional MGE that fit the modified density profile. We converted this to a two-dimensional MGE, assigning every component the common axial ratio q_{disk} , and finally repeated the same procedure for the bulge component.

Model C: The disk stars participates in the α gradient, separately from a spatially constant α_{bulge} .

Priors for all parameters are listed in Table S2. We limited the inclination to enforce intrinsic axial ratios $q > 0.05$. The anisotropy was limited to avoid non-physical JAM models that are expected when $\beta_z, \beta_r \gtrsim 0.7\epsilon_{\text{intr}} \approx 0.6$ (85). Modeling gradients in α requires physically informed priors. Spatially-resolved analyses of gravity-sensitive stellar absorption lines in low-redshift early-type galaxies have suggested that a bottom-heavy IMF produces $\alpha \approx 2.5$ in massive galaxies' centers. The most extreme cases reach $\alpha \approx 3$ (86), declining to $\alpha \approx 1.1$ at radii $R \gtrsim 0.4R_e$ (87, 88). Dynamical and lensing methods (88, 89) have similarly found $1 \lesssim \alpha \lesssim 2.5$ low-redshift early-type galaxies with $\sigma_e \gtrsim 250 \text{ km s}^{-1}$. Informed by these bounds, we set a prior range of $[0.9, 3.0]$ on all α parameters and also required $\alpha_\infty \leq \alpha_0$. As the IMF does not appear to vary appreciably at $R \lesssim 0.1R_e$ in the aforementioned samples, we fixed $r_\alpha^{\text{in}} = 270 \text{ pc} \approx 0.1R_e$ in our analysis. This enforces a requirement that α not vary at very small radii, an assumption that also underlies most M_\bullet measurements in local galaxies. We allowed r_α^{out} to vary from 540 pc (i.e., a transition over at least a factor of 2 in radius) to 5 kpc (roughly the outer bound of the kinematic data).

Following previous work (12), we traced the source kinematics through the lens mapping to the image plane and constrained the dynamical models using a Bayesian framework. The black hole was modeled as compact Gaussian whose radius we set to $\text{rbh} = 1 \text{ mas}$. Angles in the source plane were converted to distances ($1'' = 8.6 \text{ kpc}$) using our adopted cosmological parameters (90). For each spaxel i in the IFU field, we computed the positions of its corners in the source plane. We then subsampled this polygon using a 3×3 grid of points in the inner regions, or a single central point in the outer regions. At each point j , we used `jampy` to compute $V_{j,\text{rms}}$ and evaluated the surface brightness I_j of the MGE tracer model. The V_{rms}^2 value of spaxel i was then computed as the intensity-weighted mean $\sum I_j V_{j,\text{rms}}^2 / \sum I_j$, where the sums run over j , while the surface brightness of spaxel i was computed as the mean $\langle I_j \rangle$. The resulting image-plane maps of IV_{rms}^2 and I were then convolved by the NIRSspec PSF, and for each spatial bin, V_{rms}^2 was computed as the mean $\langle IV_{\text{rms}}^2 \rangle / \langle I \rangle$ over its constituent spaxels. Since this procedure models PSF convolution and pixelization, we disabled the treatment of these effects by `jampy`.

We sampled posteriors and computed the evidence Z using `UltraNest` version 4.3.3 (91, 92). We used a Gaussian likelihood and a covariance matrix Σ (Supplementary Text) that accounts for the correlations induced by resampling of the IFU data cubes. 9 of the 219 spatial bins were masked due to dust (see Stellar kinematics), local mismatch with the MGE model (see Stellar light and mass distributions), or proximity to SN Encore.

Dynamical modeling results

Marginalized posteriors for all 6 models (A-cyl, B-cyl, C-cyl, A-sph, B-sph, C-sph) are summarized in Table S2, and the M_\bullet posteriors are shown in Fig. S6. We consider the B-cyl model as the fiducial model for purposes of discussion, for illustration in Fig. 2, and as a baseline for estimating systematic uncertainties. However, our M_\bullet estimate combines results from all models. The fiducial model provides an acceptable fit, with a minimum $\chi^2 = 364$ for 210 data points and a reduced $\chi_v^2 = 1.7$, which is typical for JAM models (17). Fig. 2 also displays results from an additional model that is identical to B-cyl except that it includes no black hole, resulting in a manifestly poorer fit ($\chi^2 = 386$, $\Delta \ln Z = -12$).

M_\bullet has little covariance with parameters unrelated to α . For the fiducial model (Fig. S5), we found only upper limits to f_{DM} and no constraint on γ_{DM} . The velocity ellipsoid β_z is nearly isotropic in the center ($\beta_0 = 0.14_{-0.07}^{+0.06}$) and likely becomes more flattened with increasing distance from the

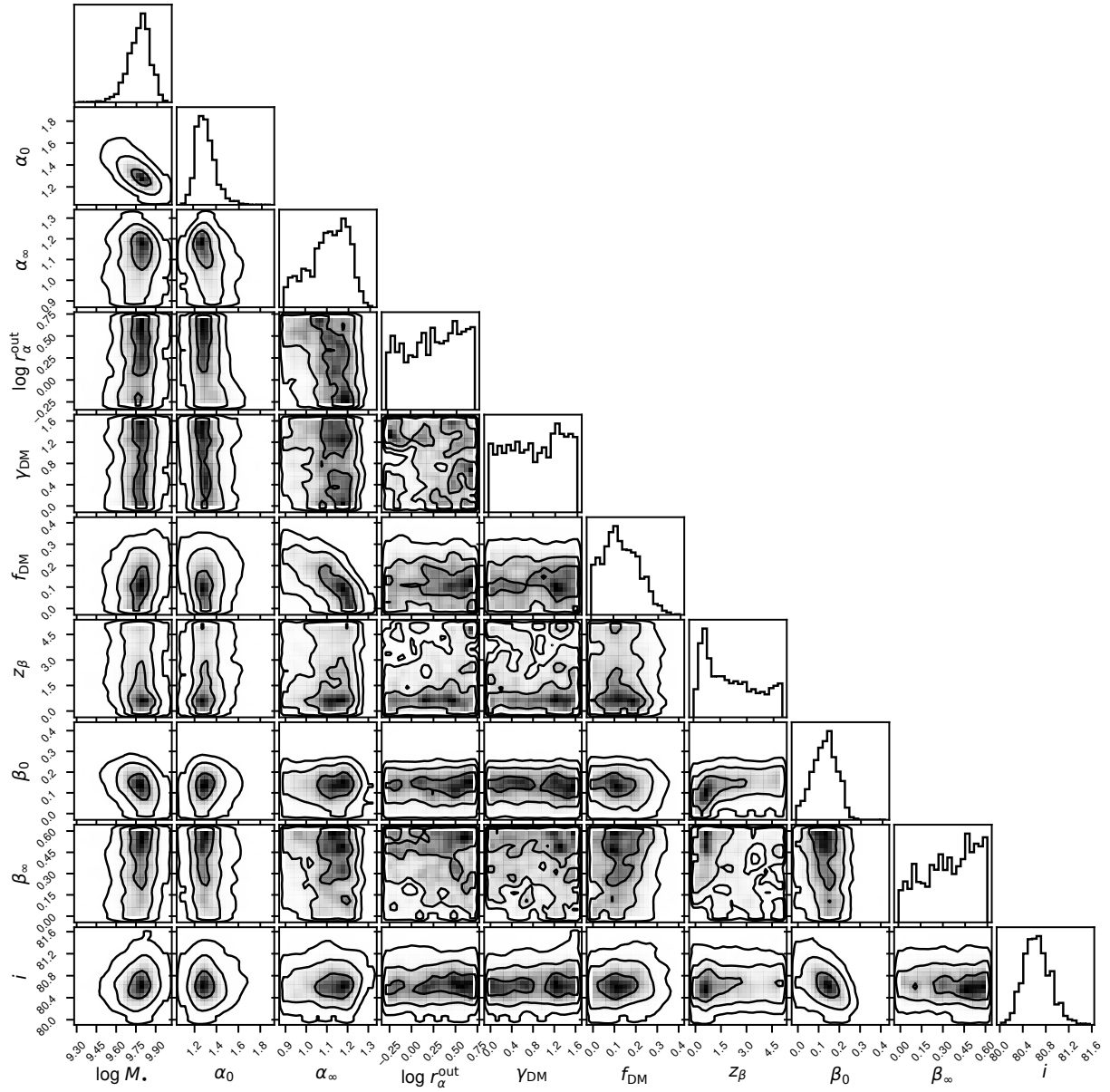


Figure S5: Posterior distributions for the fiducial dynamical model B-cyl. Marginalized 2D and 1D posteriors for each parameter are shown, with 1σ , 2σ , and 3σ contours. See Table S2 for units.

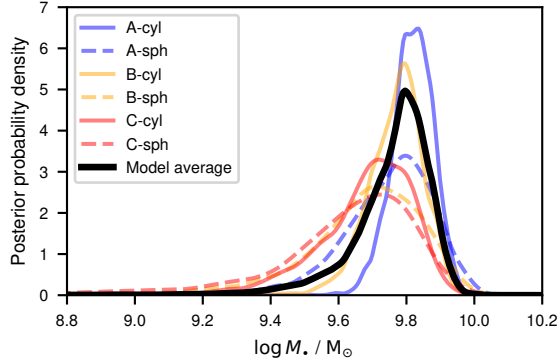


Figure S6: Marginalized posterior distributions for M_{\bullet} . Each dynamical model is shown along with the Bayesian model average from which our final estimate is derived.

equatorial plane, but M_{\bullet} has only modest covariance with the velocity anisotropy or inclination. The main covariance is between M_{\bullet} and the value of α near the center. Model A-cyl indicates little spatial variation in α , with $\alpha_{\text{disk}} \approx \alpha_{\text{bulge}} \approx 1.2$. Model B-cyl similarly indicates only a mild α gradient, if any ($\alpha_0 = 1.30^{+0.09}_{-0.07}$ and $\alpha_{\infty} = 1.12^{+0.08}_{-0.12}$). In model C-cyl, a greater range of gradients is permitted in the disk ($\alpha_0 = 1.79^{+0.57}_{-0.44}$ and $\alpha_{\infty} = 1.16^{+0.20}_{-0.17}$). This occurs because the inner disk is less well resolved than the inner bulge: it is much flatter, and its major axis is close to the direction of minimum magnification. Therefore decoupling the inner disk and bulge permits a wider range of α in the former, which in turn may affect the inferred M_{\bullet} . Model C thus provides the greatest stress test of the robustness of the M_{\bullet} measurement. The data do not favor one of models A-cyl, B-cyl, or C-cyl, which have very similar values of evidence (Table S2). The models with spherically aligned velocity ellipsoids are disfavored compared to their cylindrical counterparts by evidence ratios of 11 to 23.

All models produce compatible constraints on M_{\bullet} (Fig. S6). It is not clear *a priori* what form any IMF gradients may take, nor which alignment of the velocity ellipsoid best approximates a multi-component system. We thus considered all models to have equal prior probability, and we used Bayesian model averaging to combine their M_{\bullet} posteriors. This amounts to weighting posteriors by the evidence. The averaged posterior indicates $\log M_{\bullet}/M_{\odot} = 9.78^{+0.08+0.14}_{-0.12-0.34}$, where the two errors refer to the 68% and 95% credible intervals.

As a further test of the robustness of M_{\bullet} , we also tested a very simple dynamical model lacking dark matter and gradients in α or β_z ; the four parameters were therefore α , β_z , M_{\bullet} , and i . Although we chose not to include this restrictive model in our averaging, we note that it indicated a consistent mass $\log M_{\bullet}/M_{\odot} = 9.81^{+0.05}_{-0.06}$.

Several systematic uncertainties were evaluated by changing inputs to the fiducial model B-cyl and evaluating the resulting change to the median of the M_{\bullet} posterior: (1) To estimate the effect of uncertainties in the lens model, we isotropically rescaled the source plane coordinates and MGE dimensions by linear factors of 1.28 and 0.83, which correspond to -39% and $+44\%$ changes to μ . This shifted M_{\bullet} by $+0.10$ dex and -0.08 dex, respectively. (2) We used the alternative PSF A (Supplementary Text) and found a negligible 0.01 dex shift. (3) We uniformly changed all σ measurements by our estimated systematic uncertainty of $\pm 3\%$, which shifted M_{\bullet} by $^{+0.03}_{-0.04}$ dex. Adding these components in quadrature, we estimate a systematic uncertainty of $^{+0.11}_{-0.09}$ dex in M_{\bullet} .

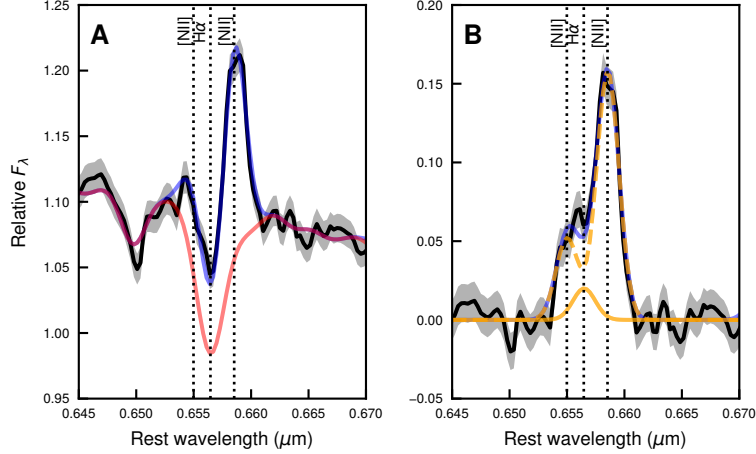


Figure S7: Nuclear spectrum constraining the H α emission. (A) The black curve and $\pm 1\sigma$ band show the observed spectrum in the vicinity of H α and [NII] $\lambda\lambda 6550, 6585$. The red curve shows the stellar continuum of the best-fit model. The blue curve shows the total best-fit model including H α and [NII] emission. (B) The black curve shows the observed spectrum with the stellar continuum of the best-fit model subtracted. The blue curve shows the total emission line model, while the orange curves show the H α (solid) and [NII] (dashed) components.

Our dynamical models neglect the mass of gas and dust. Dust continuum emission at 1.3 mm has been observed in MRG-M0138 (37), resulting in a low estimated gas-to-stellar mass fraction of 0.6% and a gas mass, given the revised magnification, of $\approx 1.3 \times 10^9 M_{\odot}$. The ALMA data do not resolve the gas distribution, but we can roughly estimate it from our maps of the dust attenuation A_V and of the equivalent width (EW) of excess Na D absorption (i.e., beyond the stellar absorption). If the neutral gas surface density is roughly proportional to A_V or EW, then $\sim 2\%$ is projected within r_{inf} . Therefore, although we do not include gas in the systematic error budget, we expect it to be dynamically negligible. In the extreme limiting case in which the gas mass is fully contained within r_{inf} and thus should be subtracted from our M_{\bullet} estimate, doing so would shift the result by $< 1\sigma$.

AGN luminosity and Eddington ratio limits

We assessed the H α luminosity $L_{\text{H}\alpha}$ in the central spaxel, corrected for aperture losses assuming point-like emission, in order to minimize the contribution from non-nuclear sources. To improve sensitivity to very weak line emission, we used $N_{\text{mult}} = 31$ in the SPS fits, corresponding to one polynomial order per 10^4 km s^{-1} . We found correlated residuals to the fitted SPS models of $\pm 1.5\%$, corresponding to the amplitude of a Gaussian emission line with a rest-frame equivalent width $\text{EW}_0 = 0.3 \text{ \AA}$ at H α . To account for this systematic, which dominates the error budget, we added 0.3 \AA in quadrature to the statistical error in EW_0 (derived from the ppxf flux error) and likewise increased the luminosity errors.

At $> 2\sigma$ significance, we detected only the [NII] $\lambda\lambda 6550, 6585$ and [OII] $\lambda\lambda 3727, 3730$ emission lines. The line ratio limits $\log [\text{NII}]/\text{H}\alpha > 0.75$ and $\log [\text{OIII}]/[\text{OII}] < -0.10$ are most consistent with a LINER spectral type. The Balmer series emission, expressed in terms of H α , was constrained to $\text{EW}_0 < 1.1 \text{ \AA}$ and $L_{\text{H}\alpha} < 10^{39.6} \text{ erg s}^{-1}$ (2σ), which we converted to a limit on $L_{\text{bol}} <$

$10^{42.1}$ erg s⁻¹ assuming a bolometric correction (18) of $C_{\text{H}\alpha} = L_{\text{bol}}/L_{\text{H}\alpha} = 300$. These estimates reflect our detection limits, but there are additional systematic uncertainties. Since we cannot constrain the Balmer decrement, we assumed that the emission lines are attenuated like the starlight ($A_{\text{H}\alpha} = 0.2$ mag). Emission lines in local LINER nuclei have low extinction; the distribution has a 2σ upper limit of $E(B - V) < 0.5$ mag (93). Based on this, we increased our upper limits to allow for possible additional extinction of $A_{\text{H}\alpha} = 1.0$ mag and for 0.3 dex uncertainty in $C_{\text{H}\alpha}$ (18), arriving at $L_{\text{bol}} < 10^{42.8}$ erg s⁻¹ and $\lambda_{\text{Edd}} < 10^{-5.1}$.

We constrained the X-ray luminosity using a 25 ks observation (Obs ID 17186) by the Advanced CCD Imaging Spectrometer (ACIS) onboard the Chandra X-ray Observatory. We used CIAO version 4.17 (94, 95) to estimate a credible interval on the model flux for point-like emission at the center of the JWST-targeted image of MRG-M0138. The spectral model was a power law with a photon index $\Gamma = 1.8$ multiplied by Milky Way absorption. The 90% credible interval on the (demagnified) luminosity in the rest-frame 2–10 keV band is $L_X = 0 - 10^{42.3}$ erg s⁻¹. Assuming a bolometric correction factor $C_X = 15.8$ (18), the credible interval for $L_{\text{bol}} = C_X L_X = 0 - 10^{43.5}$ erg s⁻¹. The X-ray non-detection thus gives a weaker limit on L_{bol} than H α but still implies a low $\lambda_{\text{Edd}} \lesssim 10^{-4.4}$.

Information on Figs. 1–3

To visualize the major- and minor-axis kinematics in Fig. 2, we selected spatial bins that overlap narrow pseudoslits along each axis. The kinematics can undergo strong gradients with a spatial bin, leading to an artificially jagged appearance due entirely to the irregular Voronoi binning scheme. We thus used the fiducial dynamical model to derive a correction for each bin, equal to the difference between V_{rms} as averaged over the full bin and as averaged over the portion of the bin within the pseudoslit. We added this correction to the observed and model V_{rms} for display purposes. White regions in Fig. 1C-D and Fig. 2B cover SN Encore and were excluded from the Voronoi binning; additional white regions in Fig. 2A indicate the bins that were ultimately masked for dynamical modeling. In Fig. 3A, for the sample from ref. (55), we computed L_{bol} and M_{\bullet} following refs. (96) and (97), respectively. For the $z \approx 2-5$ quiescent galaxies, we adopted uncertainties of 0.6 dex in M_{\bullet} , appropriate for broad-line estimates (98); in the case of ref. (31), we estimated L_{bol} following refs. (5, 96).

Table S1: Multi-Gaussian expansions of the stellar light and mass distributions. σ is measured along the major axis, which has a position angle of 215.7° .

Peak surface brightness ($L_\odot \text{ pc}^{-2}$)	σ (arcsec)	Peak surface density ($M_\odot \text{ pc}^{-2}$)	σ (arcsec)
Bulge ($b/a = 0.600$)			
4.20×10^4	0.0404	5.05×10^4	0.0291
4.06×10^4	0.0585	5.28×10^4	0.0571
4.14×10^2	0.286	1.76×10^2	0.734
2.12×10^2	0.690		
Disk ($b/a = 0.183$)			
3.93×10^5	0.00713	4.43×10^5	0.00700
9.57×10^4	0.0323	5.71×10^4	0.0240
1.61×10^3	0.111	3.52×10^4	0.0373
1.23×10^4	0.255	2.72×10^3	0.127
1.82×10^3	0.500	7.66×10^3	0.273
1.04×10^3	0.615	2.18×10^3	0.549

Table S2: Parameter constraints from dynamical modeling. Marginalized posteriors are summarized based on their shape: for f_{DM} and β_{∞} , 95% limits are given; for r_{α}^{out} and γ_{DM} , the posteriors are nearly the same as the priors and so are omitted; and for all other parameters, the median value is listed with 16–84th percentiles defining the errors. $\Delta \ln Z$ is the log evidence relative to the fiducial model. Bounds of the uniform priors are listed. The lower bounds for β_0 and β_{∞} are 0 and -1 for the cyl and sph models, respectively.

Parameter	Prior	Units	Posterior (cyl)	Posterior (sph)
Model A				
α_{bulge}	[0.9, 3]	...	$1.24^{+0.07}_{-0.07}$	$1.27^{+0.11}_{-0.13}$
α_{disk}	[0.9, 3]	...	$1.17^{+0.19}_{-0.17}$	$1.23^{+0.21}_{-0.19}$
$\log M_{\bullet}$	[8, 10.5]	M_{\odot}	$9.82^{+0.06}_{-0.06}$	$9.77^{+0.10}_{-0.15}$
γ_{DM}	[0, 1.6]
f_{DM}	[0, 1]	...	< 0.23	< 0.22
z_{β} or r_{β}	[0, 5]	kpc	$1.8^{+2.1}_{-1.3}$	$2.3^{+1.8}_{-1.5}$
β_0	[0 or -1, 0.6]	...	$0.14^{+0.06}_{-0.07}$	$0.17^{+0.15}_{-0.18}$
β_{∞}	[0 or -1, 0.6]	...	> 0.06	> -0.72
i	[79.7, 90]	deg	$80.7^{+0.3}_{-0.2}$	$81.1^{+0.3}_{-0.2}$
$\Delta \ln Z$	0.1 ± 0.7	-2.2 ± 0.8
min. χ^2	363.4	369.0
Model B				
α_0	[0.9, 3]	...	$1.30^{+0.09}_{-0.07}$	$1.36^{+0.12}_{-0.09}$
α_{∞}	[0.9, 3]	...	$1.12^{+0.08}_{-0.12}$	$1.16^{+0.09}_{-0.12}$
$\log r_{\alpha}^{\text{out}}$	[0.54, 5]	kpc
$\log M_{\bullet}$	[8, 10.5]	M_{\odot}	$9.78^{+0.06}_{-0.09}$	$9.70^{+0.14}_{-0.18}$
γ_{DM}	[0, 1.6]
f_{DM}	[0, 1]	...	< 0.26	< 0.27
z_{β} or r_{β}	[0, 5]	kpc	$1.8^{+2.1}_{-1.3}$	$2.3^{+1.8}_{-1.5}$
β_0	[0 or -1, 0.6]	...	$0.14^{+0.05}_{-0.06}$	$0.18^{+0.14}_{-0.16}$
β_{∞}	[0 or -1, 0.6]	...	> 0.05	> -0.79
i	[79.7, 90]	deg	$80.6^{+0.2}_{-0.2}$	$81.1^{+0.3}_{-0.3}$
$\Delta \ln Z$	0	-3.1 ± 0.7
min. χ^2	363.7	369.7
Model C				
α_0	[0.9, 3]	...	$1.79^{+0.57}_{-0.44}$	$1.90^{+0.60}_{-0.46}$
α_{∞}	[0.9, 3]	...	$1.16^{+0.20}_{-0.17}$	$1.22^{+0.22}_{-0.20}$
$\log r_{\alpha}^{\text{out}}$	[0.54, 5]	kpc
α_{bulge}	[0.9, 3]	...	$1.14^{+0.09}_{-0.11}$	$1.14^{+0.15}_{-0.15}$
$\log M_{\bullet}$	[8, 10.5]	M_{\odot}	$9.70^{+0.11}_{-0.16}$	$9.66^{+0.14}_{-0.23}$
γ_{DM}	[0, 1.6]
f_{DM}	[0, 1]	...	< 0.24	< 0.23
z_{β} or r_{β}	[0, 5]	kpc	$1.7^{+2.2}_{-1.2}$	$2.1^{+1.9}_{-1.3}$
β_0	[0 or -1, 0.6]	...	$0.12^{+0.06}_{-0.06}$	$0.12^{+0.16}_{-0.19}$
β_{∞}	[0 or -1, 0.6]	...	> 0.05	> -0.74
i	[79.7, 90]	deg	$80.7^{+0.3}_{-0.2}$	$81.1^{+0.3}_{-0.2}$
$\Delta \ln Z$	-0.1 ± 0.6	-2.7 ± 0.7
min. χ^2	363.5	369.3

Supplementary Text

Imaging Data Reduction

We obtained uncalibrated NIRC*am* images from the MAST archive, processed by the JWST Science Data Processing system version 2023_3a, and reduced them using the JWST Science Calibration Pipeline version 1.12.5 and context file `jwst_1180.pmap`, with snowball detection activated. We used `remstriping` (99) to remove residual striping, taking care to mask sources including the brightest cluster galaxy (BCG) of the lens. We obtained the reduced ACS image from the MAST archive and aligned it to the NIRC*am* images. Images were resampled onto a 15 mas pixel scale using Gaia DR3 (100) as the astrometric reference. For each image, we built and subtracted a model of the BCG light using `photutils.isophote` (101). Using `photutil.psf`, we built empirical PSFs from isolated stars and kernels to match the PSFs.

NIRSpec Initial Reduction and Background Subtraction

The NIRSpec observations were reduced using the JWST Science Data Processing system version 2023_3b and the JWST Science Calibration Pipeline version 1.15.1, with the context file `jwst_1276.pmap`. We activated the snowball rejection, `NSClean`, and bad pixel self-care steps. We selected the exponential modified-Shepard method (`emsm`) to resample the exposures onto an output frame with 0.05'' spaxels and north up. We found that resampling onto a smaller spaxel scale slightly improves the spatial resolution. Although it also increases correlations among nearby spaxels and the amplitude of the spectral “wiggles,” we can effectively mitigate the wiggles (see below) and account for covariances in our dynamical modeling.

The on- and off-source observations were reduced separately and registered by adjusting the `ra_center` and `dec_center` of the off-source data cubes to pixel-align them with the corresponding on-source cubes, as required for background subtraction. The G140M and G235M on-source observations were registered to sub-spaxel precision by making slight adjustments to `ra_center` and `dec_center` until a map showing the ratio of the G140M and G235M flux densities, evaluated as the median over the wavelength interval common to both gratings, was featureless. We masked the edge area that did not receive full exposure with both gratings, resulting in higher noise and poorer outlier rejection. (A NIRSpec failure required the second NIRSpec observation to be rescheduled and observed at PA rotated by 16° from the first.) The remaining area was 8.0 arcsec².

We cleaned the off-source data cubes of outlier pixels and those with elevated noise. Since the background is mostly spatially uniform, we generally formed a local background estimate by applying a 3 × 3 spatial median filter to the cleaned off-source data cube, which reduced random noise and outliers. There were, however, some regions where the background intensity was locally elevated, e.g., due to stuck-open MSA shutters. The background in such regions was removed by direct subtraction: specifically, in spaxels where the background level differed by > 10% from the median, we estimated the local background spectrum directly from the cleaned off-source data cube without applying any smoothing. Finally we subtracted this background model from the on-source data cube and propagated the errors.

Mitigating spectral wiggles

The NIRSpec detectors undersample the PSF. During data reduction images are resampled, which imprints sinusoidal fluctuations (“wiggles”) on the spectra, particularly in regions with strong flux gradients. The phenomenon has been described in detail (102). We developed a new Fourier method to model and mitigate the wiggles. Due to flux conservation, wiggles disappear as the flux is integrated over progressively larger apertures. We therefore examined the ratio between the spectrum in a given spaxel and the mean spectrum in a 5×5 neighborhood ($0.25'' \times 0.25''$) centered on that spaxel. Because MRG-M0138 has a smooth light distribution and is highly resolved, the differences between spectra separated a few spaxels are relatively subtle, and therefore the ratio spectrum is dominated by any wiggles.

Fig. S8A shows an example of such a ratio spectrum in black, with light smoothing applied. There are clear quasi-periodic modulations, whose power spectrum is shown in panel B. We aimed to isolate signal at the frequencies characteristic of wiggles while preserving signal at higher frequencies (which can arise from noise or local variations in absorption lines) and lower frequencies (which can arise from local color variations). We used a fifth-order digital Butterworth bandpass filter (`scipy.signal.butter`, (103, 104)). By examining many spaxels, we estimated critical frequencies of 0.004 and 0.018 cycles pixel⁻¹ (half the Wn parameter). Fig. S8B shows that this filter isolates the characteristic frequency range of the wiggles. The blue curve in Fig. S8A shows the result of filtering the ratio spectrum, producing a “wiggle model.” Fig. S8C demonstrates that dividing the ratio spectrum by the wiggle model cleans the spectrum of wiggles while preserving the noise characteristics and broadband features. Fig. S8D illustrates a second method for estimating the wiggles by examining the residuals from an SPS model. These residuals show a strong correlation with the wiggle model, which was derived completely independently and without reference to an SPS model, thereby validating our procedure. Fig. S8E demonstrates that, once our wiggle correction is applied, the SPS model provides a good fit.

We found that our procedure works well in spaxels with $\text{SNR} > 30$ (as estimated from the pipeline-produced noise spectrum) and applied the wiggle correction to all such spaxels. At lower SNR, the amplitude of the modeled wiggles increased rapidly. Since the lower-SNR spaxels are farther from the galaxy center, where flux gradients are generally smaller and therefore weaker wiggles are expected, the higher observed amplitudes indicate that the estimated correction is dominated by noise, so we did not apply it. We note that dewigging is not expected to bias the stellar kinematics because (1) we Fourier filter ratios of similar spectra, not the spectra themselves, and (2) the critical frequencies correspond to large velocity scales of $0.7\text{--}3.3 \times 10^4 \text{ km s}^{-1} \text{ cycle}^{-1}$.

Flux calibration corrections

To test the relative flux calibration on intermediate wavelength scales, we created an integrated spectrum of MRG-M0138 and fit an SPS model, excluding the photometric constraints. Due to the wide aperture, “wiggles” are negligible. Although the continuum shape of the model and observations agreed closely overall, we found some coherent residuals. We brought the data and models into better agreement by fitting the residuals with a 15th-order polynomial. We divided this polynomial from the spectrum in every spaxel of the data cube. This procedure removed minor percent-level continuum shape differences between the data and models on scales of $\gtrsim 2 \times 10^4 \text{ km s}^{-1}$ and so has no direct influence on the kinematics.

NIRSpec PSF

Determining the PSF of the NIRSpec IFU observations is not trivial. We followed methods similar to ref. (13) to derive the effective PSF in two ways. By default we use PSF B, but we show that using PSF A has a negligible effect on the dynamical models.

PSF A: We estimated the PSF from observations of the standard star GSPC P300-E (JWST program CAL-1538). The data were reduced using the same resampling parameters that we applied to MRG-M0138. The 4-POINT-NOD pattern differs from our observations, but it samples the same subpixel phases. For each of the G140M and G235M gratings, a PSF was built by taking the median over the wavelength range used in our SPS modeling. We then averaged the G140M and G235M PSFs and found that the result can be modeled as the sum of three anisotropic Gaussian components. The core component contains 81% of the light and has a circularized FWHM of $0.161''$. To apply the fitted PSF model to analyses of our data cube, we rotated it to maintain its orientation with respect to the instrument axes. Fitting the G140M or G235M PSFs individually changed σ by $\lesssim 10\%$, confirming that the size of the effective PSF (including pixel convolution) depends weakly on wavelength below $3 \mu\text{m}$ (13). This justifies our use of a single wavelength-independent PSF.

PSF B: We estimated the NIRSpec PSF *in situ* by degrading the NIRCcam resolution. Specifically, we rebinned the NIRCcam F200W image to match the IFU data cube and synthesized F200W photometry from the spectra. We then found the 6-parameter anisotropic Gaussian kernel (amplitude, center x_0, y_0 , dispersions σ_x, σ_y , and θ) that best matches the NIRCcam image to the synthetic NIRSpec image. Since this method does not have the flexibility to match the broad PSF components, we considered only the core of the NIRCcam PSF, which was approximated as an isotropic Gaussian with a FWHM of $0.066''$. Convolution of this by the best-fitting kernel results in an estimated FWHM of $0.127''$ for the NIRSpec PSF core, which is 21% smaller than the core of PSF A. Ref. (13) also found that an *in situ* PSF estimate produced a more compact PSF than the standard star by a similar ratio. To create PSF B, we isotropically rescaled the core component of PSF A to match the circularized FWHM of the *in situ* estimate, while maintaining the broader components.

Image-plane MGE fits

We refined the initial MGE model, which was fit to a source-plane reconstruction using `mgefit`, by fitting in the image plane. This is required to model convolution by the PSF. The model parameters were $\sigma_1, \dots, \sigma_N, q_{\text{bulge}}, q_{\text{disk}}$, and PA, where q 's represent the axial ratios and N represents the number of MGE components with `mgefit` $\sigma_i < 0.1''$. The other σ 's were fixed to their `mgefit` values, as they should be minimally affected by the PSF. Like `mgefit`, we separated these non-linear parameters from the normalizations of the MGE components, which can be quickly found by linear methods. To speed convergence, we took Gaussian priors centered on the `mgefit` values. To avoid labeling degeneracies, the prior also required that the σ_i belonging to each of the bulge and disk remain in rank order. The size of the innermost component σ_1 was ill-determined by the initial `mgefit` run that ignored the PSF, so we instead used a uniform prior with a lower bound σ_{min} , described below. For a proposed parameter set, we generated the image of each MGE component traced through the lens mapping, convolved these by the PSF, solved for the normalizations, and computed the likelihood. We used a Gaussian likelihood with errors proportional to $(F_i R_i)^{-1}$, where R_i is an elliptical radius and F_i is the surface brightness of the `mgefit` model at pixel i , which approximates the treatment by `mgefit` of equal fractional errors in logarithmic bins of radius. To

avoid diverging weights in the noisy galaxy outskirts, we enforced a floor on F_i equal to 1/300 of the maximum F_i . Finally we used `UltraNest` to find the maximum likelihood model.

`mgfit` limits the MGE components' major axis sizes to $\sigma > \sigma_{\min} = 0.75\sigma_{\text{psf}}$, because structure much smaller than the PSF cannot be reliably measured. The smaller axis of the NIRC*Cam* F200W PSF in the source plane has $\sigma_{\text{psf}} = 1.9$ mas and is oriented close to the galaxy minor axis. Therefore the smallest resolvable isophote has a semi-major axis of 1.9 mas / q . Taking the smaller axial ratio (q_{disk}) from the initial `mgfit` model then yields $\sigma_{\min} \approx 7$ mas.

Kinematic covariance matrix

The `emsm` resampling method computes each voxel in the output data cube as a weighted average of pixels in our 4 dithered exposures. The same input pixel receives appreciable weight in neighboring output voxels, particularly when resampling onto a smaller-than-native pixel scale as we do, and therefore noise is correlated in nearby spaxels. Here we derive the covariance matrix Σ that describes our V_{rms} measurements.

We first considered correlations among nearby spaxels in the output data cube in a given wavelength slice. The `emsm` weights for our configuration are $w = \exp[-(R/0.05'')^2]$, where $R = [(\Delta x)^2 + (\Delta y)^2]^{0.5}$, and Δx and Δy represent the separation between a given input pixel and a given output voxel. Furthermore $w = 0$ for $R > R_{\text{ROI}} = 0.2''$. (In detail, the weights and R_{ROI} vary with wavelength; we used values near the mid-point of our observed wavelength range.) We estimated correlations by simulation. Beginning with the first exposure, we considered a set of pixels that map onto the wavelength slice of interest. We can consider these pixels to map onto a regular grid in the output plane with a spacing of $0.1''$, which is the native pixel scale and slice width. This assumption neglects distortion, which is valid locally, and for simplicity we also neglected the rotation of the output grid with respect to instrument coordinates. We populated these pixels with Gaussian random noise. We likewise generated random noise for pixels in exposures 2–4; these map onto output spaxel grids that are shifted by $\pm 0.05''$ in each axis, reflecting the subspaxel sampling of the 4-POINT-DITHER pattern. We then constructed the output image, using the `emsm` weights described above to average the input pixels, and computed the correlation coefficient $\rho_{i,j}$ between spaxels as a function of their absolute separation $(i, j) = (|\Delta x|, |\Delta y|)$ in output spaxels. The result is only weakly sensitive to the phase of the output grid with respect to the input grids; we therefore marginalized over phase to derive

$$\rho_{i,j} = \begin{bmatrix} 1 & 0.61 & 0.14 \\ 0.61 & 0.37 & 0.08 \\ 0.14 & 0.08 & 0.02 \end{bmatrix}. \quad (\text{S2})$$

For $i, j > 2$, we approximate $\rho = 0$.

This matrix describes the spatial correlations among the fluxes in each wavelength slice of the output data cube. It also describes correlations among V_{rms} values extracted from spectra in nearby output spaxels. With correlations thus determined at the spaxel level, we finally estimated the covariance $\Sigma_{A,B}$ between V_{rms} measures extracted from two spatially binned spectra A and B :

$$\Sigma_{A,B} = \frac{\sum_{(i,j) \in A, (k,l) \in B} \rho_{|i-k|, |j-l|}}{\left(\sum_{(i,j) \in A, (k,l) \in A} \rho_{|i-k|, |j-l|} \right) \left(\sum_{(i,j) \in B, (k,l) \in B} \rho_{|i-k|, |j-l|} \right)} \sigma_A^{\text{rms}} \sigma_B^{\text{ms}}. \quad (\text{S3})$$

Here σ_A^{rms} and σ_B^{rms} represent our estimated uncertainties in V_{rms} in each bin. To arrive at this expression, we relied on linearity and further neglected flux and σ^{rms} differences among spaxels within a bin. This assumption is reasonable for the small bins of main interest; large bins composed of many spaxels are essentially uncorrelated with other bins anyway. Eqn. S3 was further verified by simulation. We used $\Sigma_{A,B}$ to compute likelihoods in our dynamical modeling.

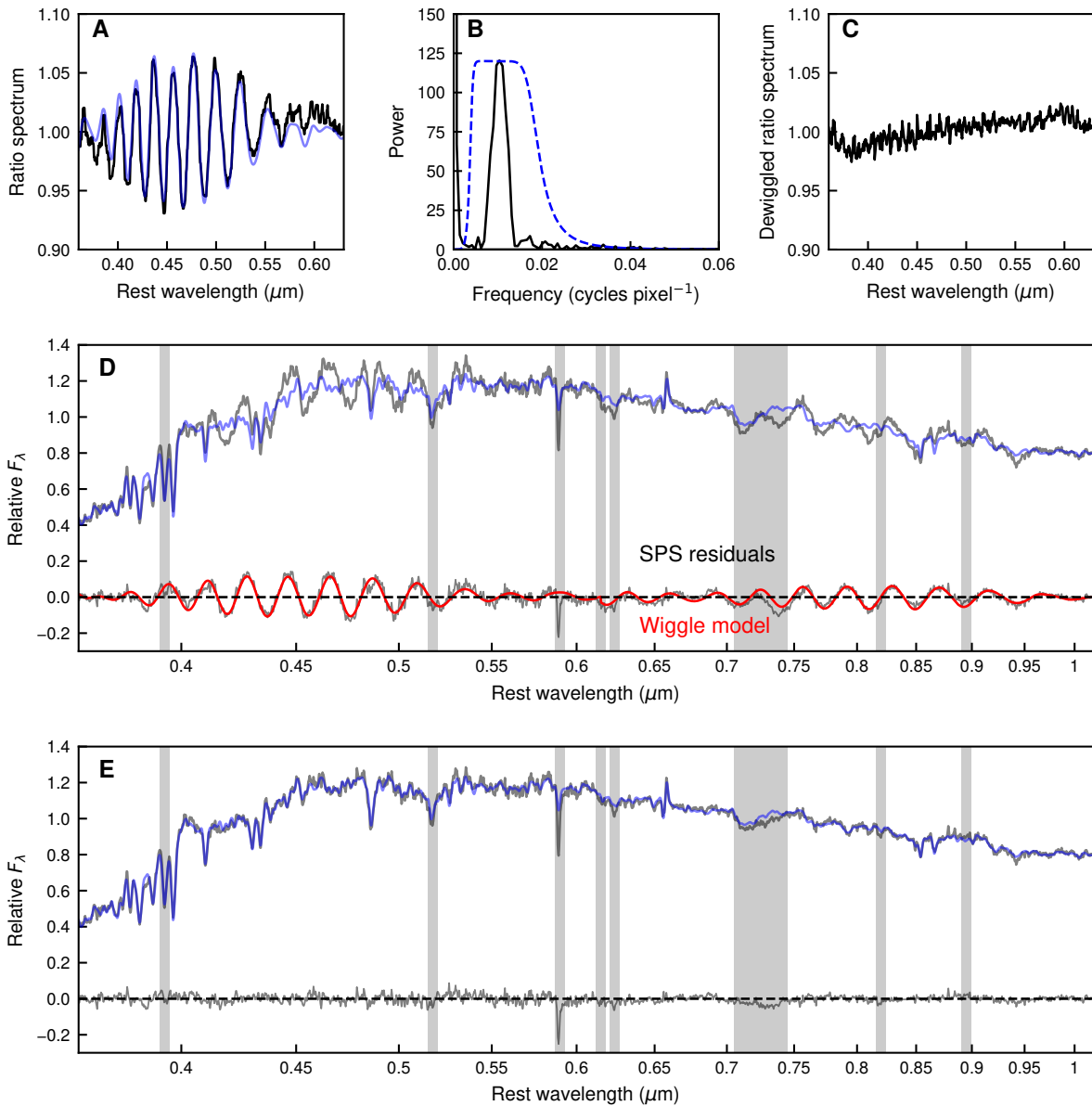


Figure S8: Modeling of spectral wiggles induced by NIRSpec undersampling. (A) An example ratio spectrum (black curve), formed by the ratio of the G140M spectrum in an example spaxel to the mean of its neighborhood, and the associated wiggle model (blue) after filtering. (B) The power spectrum of the ratio spectrum from A (black) and the Butterworth filter response (blue, arbitrary scaling). (C) The dewiggled ratio spectrum, formed by dividing the ratio spectrum and the wiggle model shown in A. (D) The full spectrum (gray) in this example spaxel, without wiggle removal applied, and a best-fit SPS model (blue). Residuals are displayed at the bottom alongside the wiggle model (red), demonstrating a good correlation. This is not a fit: the wiggle model was derived entirely independent of the SPS models. (E) The same spectrum, corrected by the wiggle model, with the best-fit SPS model and residuals. Shaded regions were masked.